THESIS

CALIBRATION OF CSU CHIVO RADAR DURING THE RELAMPAGO CAMPAIGN

Submitted by

Juhyup Kim

Department of Electrical and Computer Engineering

In partial fulfillment of the requirements

For the Degree of Master of Science

Colorado State University

Fort Collins, Colorado

Summer 2022

Master's Committee:

Advisor: V. Chandrasekar

Indrakshi Ray
Margaret Cheney

ABSTRACT

CALIBRATION OF CSU CHIVO RADAR DURING THE RELAMPAGO CAMPAIGN

Colorado State University C-band Hydrometeorological Instrument for Volumetric Observation (CSU CHIVO) radar is a dual-polarization weather radar operated by Colorado State University. CHIVO radar is easy to be transported and deployed compared to conventional S-band radars. CHIVO radar can be disassembled, shipped, and re-assembled to be deployed to observe weather phenomena at different locations in the world.

During the Remote Sensing of Electrification, Lightning, and Mesoscale/Microscale Process with Adaptive Ground Observations (RELAMPAGO) field campaign, CHIVO radar was deployed to Córdoba & Mendoza provinces in Argentina and operated during two observing periods: one from November 10, 2018, to December 22, 2018, and another from December 27, 2018, to January 31, 2019.

Any high-quality research radar requires proper calibration to ensure high data quality. To address the requirements associated with high-quality weather radar, this thesis presents 3 aspects of radar calibrations namely a) azimuth, which indicates the horizontal position of targets, b) reflectivity (Z), which indicates the returned power at horizontal polarization, and c) differential reflectivity (Z_{dr}) which indicates the ratio of the horizontal to vertical polarizations of the Z. The calibration techniques presented in this thesis utilizes the sun as a calibration source, ground targets, and meteorological targets. These three techniques are applied appropriately to analyze and calibrate the radar data sets. The goal of the radar calibrations was to improve the data quality to provide researchers with accurate data sets so that weather

phenomena under different geological and climatic conditions can be properly studied and understood.

ACKNOWLEDGEMENTS

First and foremost, I wanted to express appreciation to Dr. V. Chandrasekar who taught me valuable skills as well as interpersonal communication skills. Without his guidance, it would have been more challenging to accomplish this work. He not only guided me on my thesis but also helped me grow up as a more responsible adult.

I also sincerely appreciate Ivan Arias, Sounak Biswas, Shashank Joshil, and Ryan Gooch, who helped me improve my software development, analytical, and interpersonal skills.

I wanted to thank my colleagues and supervising Ph.D. students at the Radar and Communication Group at Colorado State University, who guided and assisted me throughout my thesis work spending their valuable time.

This research was supported by the National Science Foundation.

DEDICATION

I would like to dedicate this thesis to my academic and life advisor, Dr. V. Chandrasekar, my parents, and colleagues at CSU radar and communication laboratory, who helped me move forward during the challenging time of my life.

TABLE OF CONTENTS

LIST OF TABLES

LIST OF FIGURES

Chapter 1

Introduction

1.1 RELAMPAGO Background

Remote Sensing of Electrification, Lightning, and Mesoscale/Microscale Process with Adaptive Ground Observations (RELAMPAGO) field campaign took place in Córdoba & Mendoza provinces in Argentina and Western Rio Grande do Sul State in Brazil from 2018 to 2019. RELAMPAGO was funded by the U.S. National Science Foundation (NSF), National Oceanographic and Atmospheric Administration (NOAA), National Aeronautics and Space Administration (NASA), Servicio Meteorologico Nacional (SMN), Ministry of Education, Science and Technology of Argentina (MinCyT), Province of Cordoba, Brazil (INPE, CNPq, and FAPESP), and INVAP, S.E. During the Campaign, more than 200 scientists and graduate students from the United States, Argentina, and Brazil participated. The complex terrain of the Sierras de Córdoba & Andes causes deep convections to initiate and grow into powerful storms. These powerful storms caused intense flash flooding, severe hailstorms, extreme lightning flash rates with abnormal lightning phenomena, and a few tornadoes in the region [2]. These geological and meteorological characteristics make the region attractive for studying weather phenomena and complex precipitation microphysics.

Along the Great Plains in the U.S., abundant lower-tropospheric moisture, steep mid-tropospheric lapse rates, and strong tropospheric vertical wind shear are linked to severe thunderstorms. The weather phenomena along the Great Plains have been extensively studied, therefore, many weather forecasting models, which model the links between the terrain and the

weather phenomena have been developed. On the other hand, different characteristics such as terrains, temperature range, and soil types in Southeast South America (SESA), central Africa, and the Indian subcontinent may cause different convective storm initiation, upscale growth, and thunderstorms. Due to the different characteristics, the models developed based on the Great Plains in the U.S. may not be sufficient to explain the convective storms in the region. Aside from the space-based radar observations over the region, extensive studies involving ground-based radars have not been conducted in the region [3].

SESA has unique meteorological conditions and geographies like Great Plains The complex terrains and the meteorological conditions cause the high spatial density of convective storms in many different types, which are unique within the context of mesoscale. SESA has a long convective season spanning from spring through autumn and the complex terrains modulate the convective processes and powerful storms. These characteristics make SESA ideal to study the correlation between initiation and evolution of deep convection and complex terrain using fixed and mobile observations.

The goal of RELAMPAGO was to evaluate how consistent the hazards were associated with the weather phenomena. To evaluate the hazards associated with storms and their environments such as supercells, mesoscale convective systems, and multicell storms, both mesoscale observations from the satellite and detailed observations from the ground-based radars were compared as well as the theoretical models, which had been developed based on the Great Plains in the U.S. to compare how well the pre-existing models fit into the template of the weather phenomena in the region. By evaluating the correlations between the powerful storms, hazards, and the societal impact, the ability to monitor and predict the severe convective hazards and to anticipate changes in global convective hazard frequency and intensity under potential

future climate change scenarios have been improved continuously. These various scientific objectives have been addressed by some of the previous studies related to the RELAMPAGO field experiment [2-5]. RELAMPAGO has 5 research themes [2] as shown in Table 1.1.

Table 1.1: Research themes of the RELAMPAGO campaign, which accounted for the unique geo-climatic settings of SESA [1-5].

Research Theme	Descriptions
Convective Initiation	Evaluate how deep convections are initialized by environmental processes near the complex terrains and compare the mechanisms nearby the Sierras de Cordoba and Andes.
Severe Convective Storms	Evaluate the processes, in which meteorological, physical, and geographical environments generate hails, strong winds, and tornadoes nearby Andes and Sierras de Córdoba (SDC), and compare the processes with that of in the U.S.
Upscale growth of convection	Evaluate the kinematic, thermodynamic, and microphysical processes, which intensifies deep convections and upscale growth of the storm including those that produce tall and broad convective systems and compare these mechanisms near & apart from topography.
Lightning	Evaluate the correlations between deep convective systems and lightning, transient luminous events (TLEs), high energy emissions from thunderstorms (HEETs), characteristics across the spectrum of convective systems in and near the SDC and Andes.
Hydrometeorology	Evaluate the relationship between surface fluxes, atmospheric processes, and surface and subsurface hydrologic response in the Carcarana basin with a focus on extremes.

1.2 Focus of Thesis

In this thesis, the four techniques will be explained: attenuation correction, azimuth position calibration, relative and absolute Reflectivity (Z) bias correction using RCA and self-consistency principle, respectively, and Differential Reflectivity (Z_{dr}) bias correction. The main goal of this research is to perform calibration checks by radar antenna beam pointing correction in azimuth, Z, and Z_{dr} bias estimation based on the calibration methods mentioned above and their performance evaluation using quantitative and qualitative analyses.

This thesis covers theoretical concepts, different calibration techniques, and results produced by each radar calibration technique. Furthermore, in-depth analyses of the performance of the methods are presented to demonstrate the robustness of the calibration techniques.

1.3 Outline of Thesis

Chapter 2 presents how weather radars collect and store meteorological targets as meteorological parameters, and theoretical background on the calibration techniques. The main goal of Chapter 2 is to familiarize readers with the basics of the weather radars as well as theoretical concepts of the calibration techniques presented in this thesis.

Chapters 3, 4, 5, and 6 present details on azimuth correction, Z_{dr} bias correction, relative calibration adjustment (RCA), and the self-consistency principle, respectively. These chapters provide details on algorithms, results, and evaluations of the results using quantitative and qualitative analyses. Furthermore, the performance of each calibration technique is evaluated.

Chapter 7 provides a summary of the calibration techniques presented in this thesis and possible future work that would go beyond the work presented in this thesis.

Chapter 2

CSU CHIVO Radar Operation during the RELAMPAGO Campaign

2.1 Radar Basics

Radars are widely used to detect targets and their location, velocity, and properties. Initially, radars were mainly developed to detect incoming potential enemy targets such as aircraft and missiles during World War II. As the demand for military radars declined significantly after the war, many radars were left without potential military deployments. Over the decades, as scientists used surplus radars to observe and study complex weather phenomena, radars have been developed specifically for weather observation. One of the most notable examples is the dual-polarization radar, which transmits and receives horizontal and vertical pulses simultaneously to collect horizontal and vertical profiles of precipitations [1]. Using the more sophisticated weather radars, scientists and researchers around the world have developed weather forecasting models to improve natural disaster warning systems, which reduce infrastructural damages and casualties caused by natural disasters.

Weather radars are remote sensing instruments capable of observing precipitation over a large area. They are very useful for monitoring severe weather conditions in urban areas as well as complex terrains where the deployment of in-situ instruments are not feasible [7-10]. Historically weather radars used to be ground-based, however, with the advancement in technology weather has been deployed onboard satellites such as the Global Precipitation Measurement (GPM) mission core-satellite [11-14]. Spaced-based weather radars have the

advantage to observe remote locations on earth. Weather radars have been widely used to detect and study precipitations. The transmitted Electromagnetic (EM) waves get scattered from hydrometeors such as raindrops, and the backscattered waves are received by the radar [1]. This phenomenon is called "Rayleigh scattering". The frequency of the radar is chosen based on the desired sensitivity and the cost of radar for weather applications. For example, Ka-band radars (1-cm wavelength) are highly sensitive and used for detecting smaller particles such as clouds, and X-band radars (3-cm wavelength) are used as gap-filling radars for short-range applications. On the other hand, a 10-cm (S-band) radar does not suffer from attenuation significantly, therefore, is ideal for weather monitoring over a large region, however, the S-band (10-cm wavelength) radar comes with a high price tag. Considering the trade-off, a C-band radar (5-cm wavelength) can be desirable as it is easy to be deployed and cost-effective, yet it suffers from a certain level of attenuation compared to an S-band radar.

The transmitted EM pulses spread out as they travel along the path and cover a larger volume of the area at farther ranges with lower resolution. For an S-Band radar, typically, a single pulse covers an area on the order of a cubic kilometer at the end of the 150-km sounding range. In addition, at very distant ranges beams tend to overshoot cloud tops. For this reason, the maximum range of 150 km is chosen for atmospheric measurements. Higher frequencies tend to get more attenuated due to precipitation medium. For example, typical ranges for X-Band are 40 km.

Referring to [1], the radar-target radial range R in terms of the speed of light c and time t is described as

$$R = \frac{ct}{2} \tag{2.1}$$

Meteorological targets that consist of raindrops, snow, and/or hails travel in different directions with varying velocities. Therefore, meteorological radars collect the distributed targets within a sample volume. This is defined by the radar's vertical and horizontal beamwidths θ and ϕ, respectively, over the sample range Δr [1]. The sample range Δr can be expressed in terms of pulse duration, T_0, as

$$\Delta r = \frac{cT_0}{2} \tag{2.2}$$

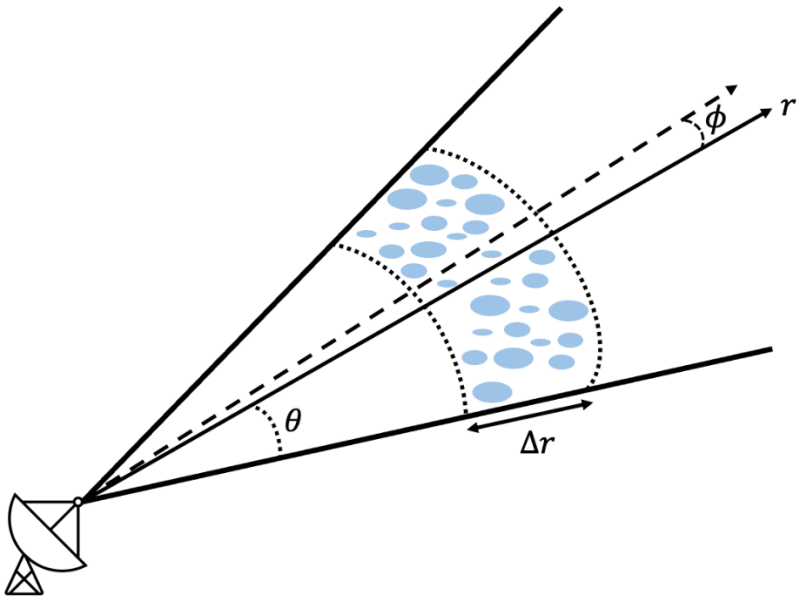

Figure 2.1: Distributed meteorological targets within a defined volume [1].

r_{max} is defined as the maximum range a radar signal travels and returns before the next radar signal is transmitted. In other words, the pulses returned from closer than r_{max} away from the radar are unambiguous. Referring to [1], r_{max} can be written in terms of c and pulse repetition time T_s as

$$r_{max} = \frac{cT_s}{2} \tag{2.3}$$

The V_{max} is the maximum velocity of distributed targets a radar can detect unambiguously and can be expressed in terms of T_s and the radar wavelength λ [1]. Therefore, V_{max} can be expressed as

$$V_{max} = \pm \frac{\lambda}{4T_s} \tag{2.4}$$

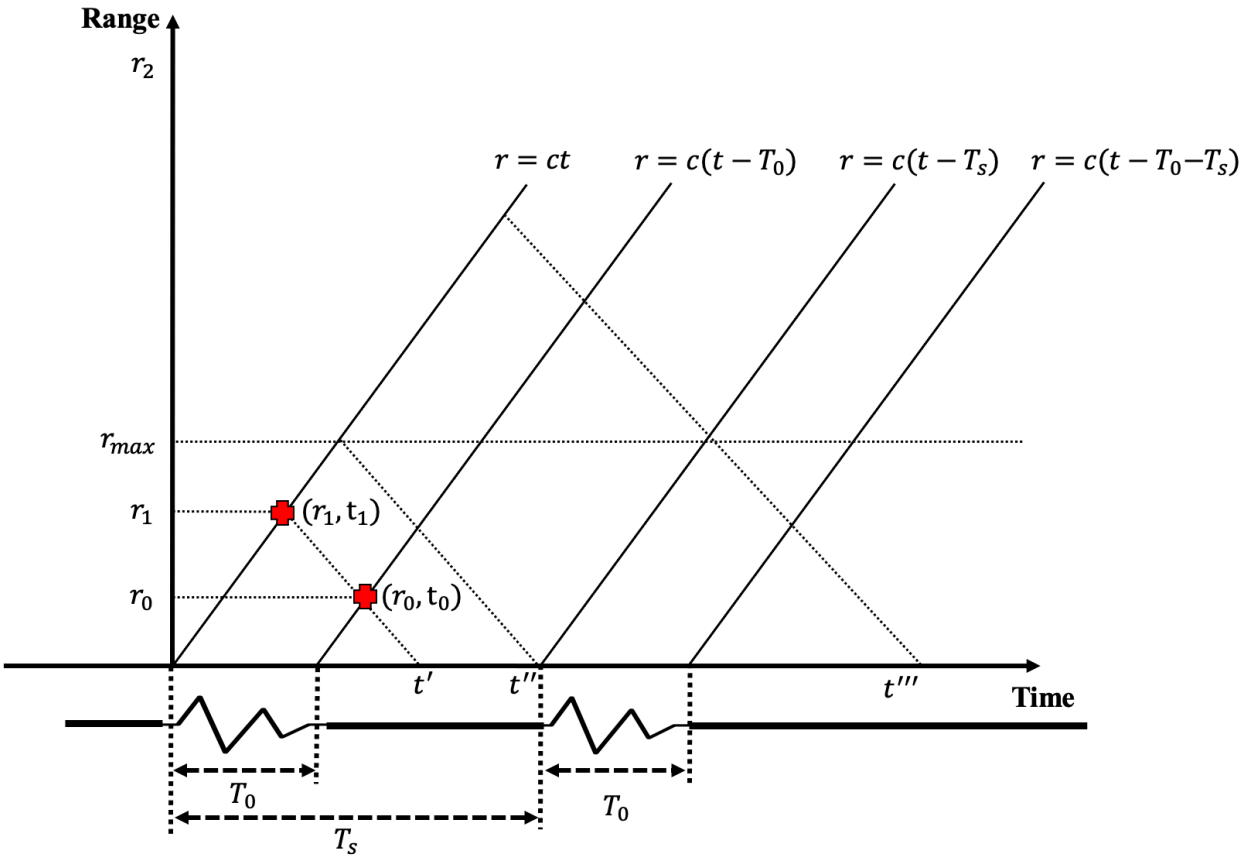

Figure 2.2: The relationship between range and time for a radar system [1].

Although a radar receives signals that travel farther than r_{max}, the returned signals beyond the r_{max} include signals from two or more pulses that were transmitted. In other words, the returned signals at t''' would contain signals from the two pulses: one between $t = 0$ and T_0, and another between $t = T_s$ and $T_s + T_0$, which makes the signals ambiguous [1]. This phenomenon is called range folding. Since the unambiguous maximum range and velocity r_{max}

and V_{max} are inversely proportional in terms of the pulse repetition time T_s, sending signals with lower T_s would increase r_{max} while decreasing unambiguous velocity V_{max} for the targets within the sample range Δr [1]. This phenomenon, which causes the trade-off between either r_{max} or V_{max} while degrading the other is called Doppler Dilemma. Due to the Doppler Dilemma, an optimal T_s is typically chosen depending on the wavelength of the radar and the desired r_{max} and V_{max} to be achieved. For example, for a 5-cm C-band radar, increasing the maximum unambiguous velocity from 12.5 m/s to 18.75 m/s degrades the maximum unambiguous range from 150 km down to 100 km. The reason why an S-band radar is ideal is that as V_{max} is proportional to the wavelength, the S-band radar can achieve a higher V_{max} than a C-band radar with the same r_{max}.

Nevertheless, due to the cost-effectiveness and the radar data calibration techniques that allow correcting the radar data, C-band radars are popular among many research institutes worldwide. Details on radar technology are out of the scope of this thesis. This thesis covers software-based techniques that calibrated the data produced by the C-band CSU CHIVO radar.

There are two types of weather radar scans: plan position indicator (PPI) and range height indicator (RHI) [1]. PPI refers to a meteorological radar scanning technique, which positions a radar at a fixed elevation angle and rotates the radar horizontally. For PPI scans, a radar is typically rotated 120, 240, and 360 degrees horizontally, and the elevation angles are typically chosen between 0.5 and 90 degrees. During the RELAMPAGO campaign, the CSU-CHIVO radar was configured to operate at appropriate azimuth directions and at certain elevation angles with respect to ground to collect as much weather data as possible. RHI refers to another meteorological radar scanning technique, which positions a radar at a fixed azimuth and allows the radar to scan vertically from 0.5 to 90 degrees. RHI scans are widely used by research

institutes, where vertically scanned precipitation data allows researchers to understand a variety of weather phenomena. For RHI scans, the radar is positioned at a few azimuths between 0 and 360 degrees, and the radar scans vertically from 0.5 to 90 degrees. During the RELAMPAGO campaign, 120 and 270-degree PPI scans were optimally utilized to increase the sampling rate of the precipitation data. As a result, the CSU-CHIVO radar scanned light and heavy precipitation, ground targets, and solar and radiofrequency (RF) rays that were utilized to calibrate azimuth, Z, and Z_{dr}.

The details of radar signal processing and dual-polarization weather radar systems are beyond the scope of this thesis. For the details on weather radars, one can refer to an excellent book on the principles and applications of polarimetric Doppler meteorological radar ([1]: Chapter 5).

2.2 Radar Parameters in Meteorology

2.2.1 Reflectivity

Reflectivity (Z) [$1mm^6/m^3$], is a meteorological radar product, which describes the characteristics of rain medium [1]. Z is commonly expressed in terms of decibels relative to Z (dBZ), which allows Z to express a variety of precipitation conditions easily, including light precipitation to heavy precipitation with hails [15]. Specifically, Z describes the density of droplets within a defined volume, where the low and high values of Z indicate light and heavy precipitation, respectively. Z can be divided into two parameters: Z_h and Z_v, which are Z obtained by radar signal pulses in horizontal and vertical orientations, respectively. Subscript Z is commonly used to indicate Z_h, due in part to Z_h being directly proportional to the heaviness of precipitations because raindrops in heavy precipitations are oblate-shaped, therefore, more radar

signal pulses in horizontal orientation are returned to the radar. In this thesis, subscript Z will be used to indicate Z_h. The value of Z between 5 and 27.5 dB indicates light precipitation, between 27.5 and 42.5 dB indicates heavy precipitation, and between 42.5 and 55 dB indicates heavy precipitation. When the value of Z is above 55 dB, it indicates that hails are present with heavy precipitation [16]. Table 2.1 shows how the value of Z with types of precipitation events.

Table 2.1: The range of Z versus characteristics of precipitation [16].

Value of Z [dB]	**Precipitation Scenario**
5 < Z < 27.5	Light precipitation
27.5 < Z < 42.5	Moderate precipitation
42.5 < Z < 55	Heavy precipitation
Z > 55	Heavy precipitation with hails

The radar product Z can be expressed in terms of characteristics of rain medium, radar parameters, and attenuation. The most widely used parameter to describe microphysical properties of rain medium is raindrop size distribution (DSD) [1]. DSD models the number of estimated raindrops present within a defined spherical volume in 3-D space [17]. To account for natural variations within the rain medium, a normalized gamma distribution model is used to describe the raindrops within the volume [18]. DSD, denoted by $N(D)$, describes the number of raindrops per unit size interval as

$$N(D) = N_0 f(\mu) D^{\mu} \exp\left[-(3.67 + \mu)\frac{D}{D_0}\right] \tag{2.5}$$

$$f(\mu) = \frac{6}{3.67^4}\frac{(3.67 + \mu)^{\mu+4}}{\Gamma(\mu + 4)} \tag{2.6}$$

Where Γ is the gamma function, D_0, N_0, μ are gamma distribution parameters that model raindrop sizes, numbers, and shapes, respectively, and $f(\mu)$ is the gamma distribution function to model DSD to account for a variety of precipitation conditions.

To account for the characteristics of water, the dielectric factor of water [18] K_w can be defined as

$$K_w = (\epsilon_r - 1)/(\epsilon_r + 2) \tag{2.7}$$

Where ϵ_r is the complex dielectric of water.

Since Z is one of the standardized radar products, radar parameters are considered to produce consistent Z datasets regardless of different radar parameters. This is because weather radars have different specifications for different uses, such as operating frequencies [19]. Combining DSD, wavelength, and radar cross-sections, Z at horizontal and vertical polarization is defined as

$$Z_{h,v} = \frac{\lambda^4}{\pi^5 |K_\omega|^2} \int_{D_{min}}^{D_{max}} \sigma_{h,v}(D) N(D) dD \ [mm^6 m^{-3}] \tag{2.8}$$

Where $\sigma_{H,V}$ represents the radar cross-sections at horizontal and vertical polarizations, λ is the wavelength of the radar, K_ω is the dielectric factor of water, $N(D)$ is DSD, and D is the volume of spherical raindrops in millimeter.

Electromagnetic waves transmitted by the radar are absorbed and scattered by raindrops within rain media. This phenomenon provides valuable information on phase delays, yet, as far as Z is concerned, the phenomenon causes attenuation, which must be corrected. To correct attenuation, an attenuation coefficient can first be introduced in terms of DSD and radar cross-sections. For this reason, specific attenuation ($\alpha_{h,v}$) is used to describe attenuation at vertical and horizontal polarization [19]. This is obtained by observing the power loss of the radar signals at

both polarizations. Combining DSD, the power loss ($\sigma_{ext(H,V)}$), and the specific attenuation at vertical and horizontal polarizations, $\alpha_{H,V}$ can be defined as

$$\alpha_{h,v} = 4.343 \times 10^{-3} \int_{D_{min}}^{D_{max}} \sigma_{ext(H,V)}(D)N(D)dD \; [dBkm^{-1}] \tag{2.9}$$

Furthermore, the α_{DP} [19] describes the difference between attenuation at horizontal polarization and vertical polarization as

$$\alpha_{dp} = \alpha_h - \alpha_v \tag{2.10}$$

Where $\sigma_{ext(h,v)}$ is the extinction cross-section m^2, which indicates the total power loss, which is caused by scattering and absorption.

Positive α_{DP} indicates that there is more attenuation at horizontal polarization than vertical polarization [19]. Using the specific attenuation $\alpha_{H,V}$, two-way cumulative attenuation can be defined, which is obtained by taking the integral of the specific attenuation along the propagation path [20]. The cumulative attenuation at horizontal polarizations along the propagation path r_0 to r can be expressed as

$$A_h = 2 \int_{r0}^{r} \alpha_h(s)ds \tag{2.11}$$

The ratio of the horizontal to vertical cumulative attenuation can be expressed as

$$A_{dp} = 2 \int_{r0}^{r} \alpha_{dp}(s)ds \tag{2.12}$$

Considering the properties of raindrops, radar parameters, and the attenuation coefficients, Z at horizontal and vertical polarizations can be defined in terms of the measured Z, which is denoted as Z_m [20]. Therefore, the intrinsic Z can be expressed as

$$Z(r) = Z_m(r)e^{-0.46 \int_0^r \alpha_{h,v}(s)ds} \tag{2.13}$$

2.2.2 Differential Reflectivity (Z_{dr})

Differential reflectivity (Z_{dr}) represents helps the estimation of the shape and orientation of meteorological targets. It is the ratio of the horizontal to the vertical returned power in dB units [1]. The possible range of values of Z_{dr} is ±7.9 dB. Positive Z_{dr}indicates the returned signal power is greater for the horizontal polarization compared to the vertical polarization. This means the hydrometeors are oblately shaped (the major axis is horizontally orientated) such as large rain drops. Negative Z_{dr}indicates greater returned signal power in the vertical polarization compared to the horizontal polarization. This is the case for prolate-shaped hydrometeors. An example would be ice crystals oriented vertically by the electric field that raindrops are taller than wide. In an advanced weather interactive processing system (AWIPS), if the Z_{dr} data points are lower than -4 dB, the Z_{dr} data points are presented as approximately -3.956 dB. It is uncommon for Z_{dr} to be largely negative for typical meteorological targets with a few exceptions such as horizontally oriented hails, debris from tornadoes, small vertically oriented hails, and large hydrometeors horizontally oriented objects due to the Mie scattering effect.

In terms of the ratio of the horizontally and vertically oriented Z written as Z_h and Z_v, respectively, Z_{dr} is expressed as

$$Z_{dr} = 10 \log\left(\frac{Z_h}{Z_v}\right) dB \tag{2.14}$$

The vertical to the horizontal ratio of raindrops $\frac{b}{a}$ describes the shapes of raindrops in terms of the spherical diameter of a raindrop [21]. The ratio of the vertical to horizontal of raindrops can be express as

$$\frac{b}{a} = 1.03 - 0.062 D_e \tag{2.15}$$

Where D_e is the spherical diameter of a raindrop in millimeters and a and b are the semimajor (horizontal) and semi-minor (vertical) axis of the raindrop.

Z can also be expressed in terms of radar parameters and the microphysical properties of water [20]. Using DSD, radar cross-section, wavelength, and dielectric of the water, horizontal and vertical Z ($Z_{h,v}$) can be re-written as

$$Z_{h,v} = \frac{\lambda^4}{\pi^5 |K|^2} \int \sigma_{h,v}(D) N(D) dD \; [mm^6 m^{-3}] \tag{2.16}$$

Where $= \frac{\epsilon_r - 1}{\epsilon_r + 2}$, ϵ_r is the dielectric constant of water, $\sigma_{h,v}$ is radar cross-sections at horizontal and vertical polarizations, and $N(D)$ is DSD.

Z_{dr} can be expressed in terms of radar cross-section at horizontal polarization and vertical polarization in combination with DSD [21]. By separating the radar cross-sections at horizontal and vertical polarizations, Z_{dr} can be written as

$$Z_{dr} = \frac{\int \sigma_h(D) N(D) dD}{\int \sigma_v(D) N(D) dD} [dB] \tag{2.17}$$

Drizzle drops, which are close to being spherical reflect approximately the same vertical and horizontal pulses back to the radar. In other words, Z_h and Z_v return the same value, which makes the ratio of Z_h to Z_v become 1. Since Z_{DR} is in the dB scale, the value of Z_{dr} becomes 0. When larger raindrops are falling from the sky, the drops are dragged by the air, therefore, becoming oblate-shaped. Due to the shapes of the raindrops, the drops reflect more horizontally oriented pulses back to the radar. As a result, the radar observes Z_h higher than Z_v, therefore, the value of Z_{dr} becomes positive. Thus, Z_{dr} increases with larger hydrometeor size. In contrast, vertically long ice crystals reflect stronger vertical pulses than horizontal pulses to the radar. This makes the ratio of Z_h to Z_v less than 1, therefore, the value of Z_{dr} becomes negative on the dB scale.

Z_{dr} is used to classify the meteorological targets as well as non-meteorological targets such as rain, snow, hails, melting layers, debris, ice crystals, and birds and insects. Z_{dr} ranges from 0 to approximately 3 dB for the pure raindrops depending on the size; Z_{dr} increases as the size of the raindrops increases while the air drags cause the raindrops to be oblate-shaped, causing the droplets to return higher power horizontally than vertically. Updraft, where liquid raindrops are lofted while being oblate-shaped, can be identified by localized Z_{dr} above 2 dB within supercells.

Ice crystals form 3 different shapes: vertically oriented, horizontally oriented, and relatively spherical. Z_{dr} for typical ice particles including typical snow is between 0 and 0.5 dB because the ice crystals are distributed with lower density compared to liquid raindrops. On the other hand, for densely distributed ice crystals, Z_{dr} becomes above 1 dB. Positive Z_{dr} is also observed for the melting layers, as the melting ice becomes horizontally oriented before completely melting. For this reason, melting layers are typically identified by the Z_{dr}, which would be shown the higher values along the horizontal line. Typical smaller horizontally oriented hails less than 5.08 cm in size return negative Z_{dr} with Z between 60 and 65 and relatively larger hails return Z_{dr} between 0 and 1 dB. For non-liquid and large objects, the Mie scattering effect causes the sign of Z_{dr} to flip. For this reason, horizontally and vertically oriented hails larger than 5.08 cm return negative and positive values of Z_{dr}, respectively. For the same reason, large non-meteorological targets such as birds return Z_{dr} from -3 dB to -2 dB and from 6 dB to 7 dB. In contrast, since the Mie scattering effect does not occur for smaller targets, the value of Z_{dr} ranges from 1 to 7.9 dB, and the negative Z_{dr} is typically not observed for insects. Other non-meteorological targets such as tornadic debris can be observed by localized depressed Z_{dr} due to the debris detected by radar vertically oriented.

Another characteristic of Z_{dr} to be noted is the depolarization effects. As the radar pulses are transmitted, horizontal-oriented pulses return as horizontal-oriented pulses. This effect is commonly observed by spikes of high and/or low Z_{dr} along the propagation path. Figure 2.3 shows the shape of the droplets, the corresponding range for Z_{dr}, and typical precipitation types.

Z_{dr} Explainations	Spherical	Horizontally Oriented	Vertically Oriented
Shape of the Target		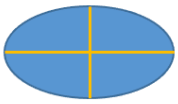	
Z_h vs Z_v Comparison	$Z_h \cong Z_v$	$Z_h > Z_v$	$Z_h < Z_v$
Z_{dr} Range	$Z_{dr} \cong 0\ dB$	$Z_{dr} > 0\ dB$	$Z_{dr} < 0\ dB$
Meteorological Target Examples	Light raindrops & small hails.	Large raindrops & melting hails.	Vertically-oriented ice crystals.

Figure 2.3: 3 types of raindrops and their corresponding Z and Z_{dr} characteristics and meteorological target examples.

2.2.3 Differential Phase (ϕ_{dp})

As the radar pulses pass through rain media, the media slow down the radar signals and the delays from the returned signals are observed on the radar. For dual-polarization radars, phase delays at horizontal and vertical polarizations can be observed separately [1]. For this reason, the difference between the phase delays at horizontal and vertical polarizations provides more information on the precipitation profiles. Using this principle, a radar parameter, which

represents the cumulative phase delays along the propagation path can be used to evaluate precipitation profiles. This parameter is called the differential phase, denoted by a symbol ϕ_{dp}.

ϕ_{dp} is one of the dual-polarization radar products, which indicates cumulative phase delay in terms of the ratio of horizontal to vertical polarization along the propagation path [21]. ϕ_{dp} is used for a variety of applications in meteorology including identifying characteristics of rain media and correcting other radar parameters such as Z [22]. For example, horizontally oriented raindrops return positive ϕ_{dp} and vertically oriented ice crystals return negative ϕ_{dp}. On the other hand, spherically oriented objects such as drizzles and hails would return ϕ_{dp} of 0 deg/km. For typical heavy precipitations, where raindrops are horizontally oriented, phase delays occur more at horizontal than vertical polarization, which returns a higher value of ϕ_{dp} [23]. Mathematically, ϕ_{dp} in deg/km can be expressed as

$$\phi_{dp} = \phi_h - \phi_v \tag{2.18}$$

Where, ϕ_h and ϕ_v are horizontal and vertical differential phase shifts, respectively.

For heavy precipitations, which include horizontally oriented raindrops, ϕ_{dp} keeps increasing along the propagation path while staying constant along the path where no targets are located. Therefore, the slope of ϕ_{dp} along the path indicates how much phase delay occurs at that location [24]. As shown in Figure 2.4, for heavy precipitations, ϕ_{dp} increases from r_0 to r', stays constant from r' to r'', and increases again from r'' to r'''.

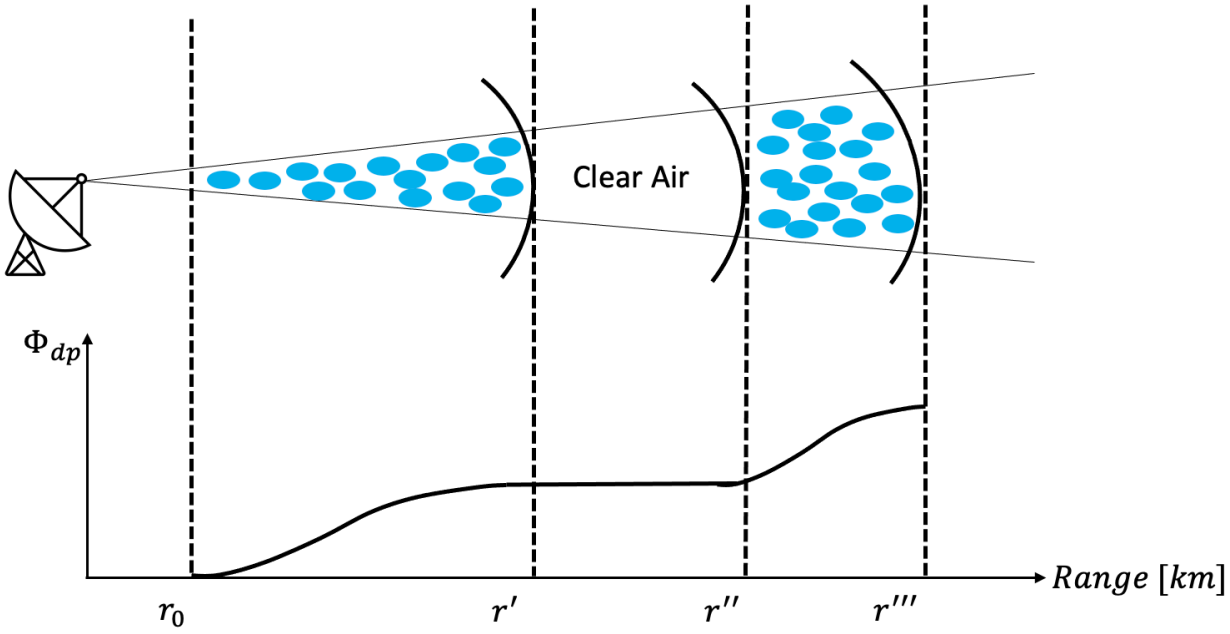

Figure 2.4: ϕ_{dp} characteristics along the propagation path where rain cells separated by the clear air are present.

2.2.4 Specific Differential Phase (K_{dp})

K_{dp} is a range derivative of ϕ_{dp}. In other words, K_{dp} indicates the phase delays that occur at each range location due to rain media, which consists of horizontally oriented raindrops [1]. In meteorology, with the possible range between -2 and 7 deg/km, K_{dp} is used for identifying the types of meteorological targets as well as estimating the rain rates. K_{dp} can be defined as the integral of ϕ_{dp} [21]. In terms of ϕ_{dp}, K_{dp} can be described as

$$K_{dp} = \frac{\phi_{dp}(r_2) - \phi_{dp}(r_1)}{2(r_2 - r_1)} \tag{2.19}$$

The main advantage of K_{dp} over ϕ_{dp} is that rain media using K_{dp} can be more easily interpreted. This is because ϕ_{dp} accumulates when rain media cause phase delays along the propagation path and the slope of ϕ_{dp} indicate where the delays occur, therefore, it is more

difficult to interpret where the phase delays occur. As shown in Figure 2.5, K_{dp} shows where the precipitation is located and how much phase delay occurs horizontally more than vertically.

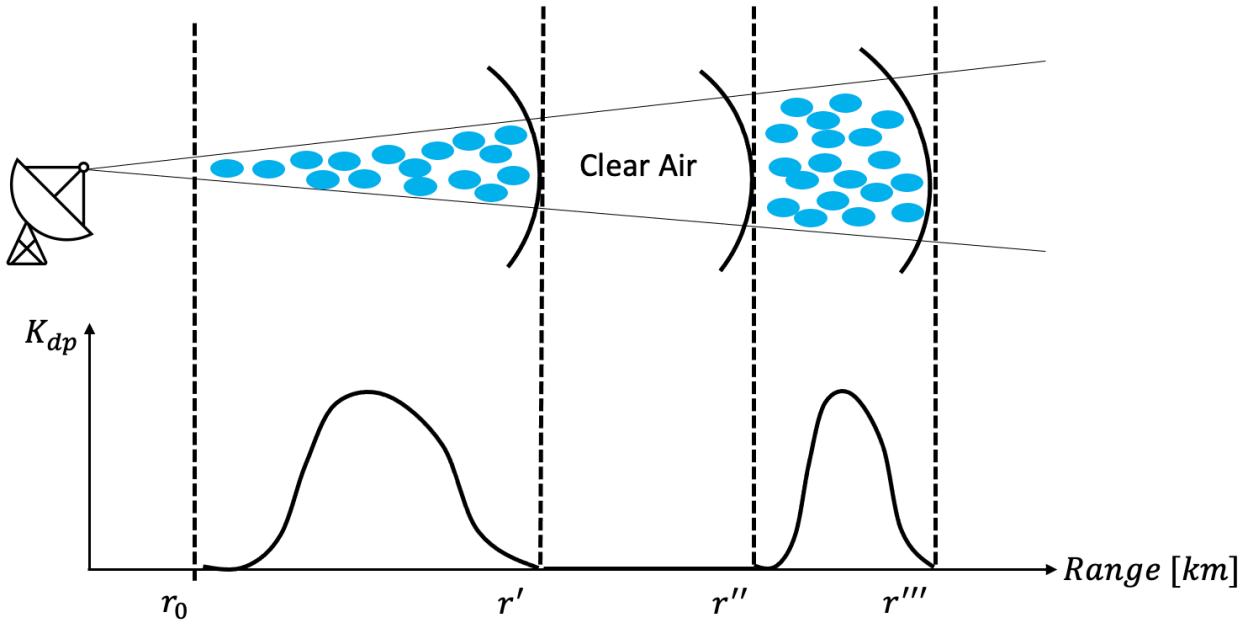

Figure 2.5: K_{dp} characteristics along the propagation path where rain cells separated by the clear air are present.

The more densely distributed oblate-shaped objects are present, the more phase delays occur at the horizontal polarization. In meteorology, the most common example is large falling oblate-shaped raindrops. On the other hand, hails are typically in a spherical shape, therefore, do not cause K_{dp} to increase. Taking advantage of these characteristics, K_{dp} can be used to distinguish rain, hail, and mixed conditions in combination with Z and Z_{dr}, which would be difficult to classify with Z and Z_{dr} alone. Generally, raindrops and hail return K_{dp} from 0 and 7 deg/km and – 0.5 to 1 deg/m, respectively. This is because the horizontally oriented raindrops would cause the pulses to slow down horizontally more so than vertically, and spherical-shaped hails would cause the same delays vertically and horizontally. Similarly, snow, which is relatively spherically shaped returns K_{dp} between 0 and 0.5 deg/km. Finally, ice crystals, which are typically horizontally oriented, but occasionally vertically oriented return K_{dp} between -1 and

0.75 deg/km. Although K_{dp} itself provides useful information on classifications of meteorological targets, it is important to consider Z, Z_{DR}, and K_{DP} characteristics altogether to classify the targets correctly. For example, for heavy rain precipitations with Z nearing 50 dBZ, Z_{dr} and K_{dp} range from 3 to 4 dB and 1 to 2 deg/km, respectively. On the other hand, hails would return Z nearing or above 50 dBZ, and Z_{dr} and K_{dp} nearing 0 dB and 0 deg/km, respectively. This is because hails are typically spherical. In contrast, Z above 50 dBZ, Z_{dr} between 3 and 4 dB, and K_{dp} nearing 5 deg/km would indicate either melting hail, which is oblate-shaped, or a large amount of falling liquid raindrops.

Warm and cold precipitations can be identified with K_{dp} in combination with Z and Z_{dr}. Warm precipitations include smaller raindrops with high raindrop distributions, which would be indicated by relatively low Z_{dr} with high K_{dp}. For example, Z_{dr} between 1.5 and 2.5 dB with higher K_{dp} would indicate warm precipitations. In contrast, higher Z_{dr} near 3 dB in combination with lower K_{dp} would indicate cold precipitations. The specific temperature of the atmosphere can be further verified by soundings, however, K_{dp} is a useful parameter to be used to classify the temperature over the area where the precipitation is present.

The accuracy of K_{dp} degrades significantly when the correlation coefficient (σ_{hv}) is lower than 0.9. Therefore, in typical weather applications, for the data points with σ_{hv} less than 0.9, K_{dp} is not computed. Furthermore, the lower the signal-to-noise ratio (SNR), the lower the confidence of K_{dp} becomes, therefore, K_{dp} over these data points must be disregarded. Non-uniform beam filling (NBF) occurs when significant gradients of ϕ_{dp} occur within a pulse volume, where the lines of storms align along a radial. This can be observed by the low σ_{hv}. The

data points over the area affected by NBF do not produce reliable K_{dp}, therefore, K_{dp} is not computed over this area.

2.3 Theoretical Background

2.3.1 Azimuth Correction

During the RELAMPAGO campaign, continuous operation of CHIVO radar collected solar, RF rays, and ground targets, and the motion of the rays and the ground targets were observed. The motion of the targets was caused by the rotation of CHIVO radar itself, therefore, indicating that the azimuth readings from the radars were incorrect. Although the azimuth was corrected on-site during the campaign, the azimuth biases degraded the performance of RCA because it collected and calculated Z bias using location-dependent ground targets.

To correct the azimuth datasets, the solar and RF ray locations were verified by observing the characteristics of the rays. This was achieved by plotting 3-degree PPI and analyzing the Z characteristics of the rays along the propagation path. For both solar and RF rays, Z gradually increased from 0 to 5 dB between the 80 and 150-km range. When the ray locations were verified, the azimuth readings of the targets from CHIVO radar were recorded. The positions of the solar rays were then compared to the actual solar ray positions provided by NOAA Solar Position Calculator at the time at the location where and when CHIVO radar was positioned. As a result, the target positions were drifting clockwise, which indicated that CHIVO radar was drifting counterclockwise. Tracking RF rays and ground targets provided data on how much the radar was drifting each hour relatively. On the other hand, tracking the solar rays at sunrise and sunset provided the absolute azimuth error of CHIVO radar. Using these datasets, both the

hourly and daily azimuthal drift of CHIVO radar were recorded and the azimuth datasets were corrected.

2.3.2 Attenuation Correction

The radar signals along the propagation path where rain media are present absorb part of the signals and cause them to scatter. As a result, the signals returned to the radar become weaker than the transmitted signals. The signal loss causes lower measured datasets for Z and Z_{DR} than their intrinsic counterparts [1]. In meteorology, this phenomenon is called attenuation.

Attenuation can be calculated by observing the phase delays. For dual-polarization radars, K_{dp} is used to describe the phase delays at each range location along the propagation path [15]. Using K_{dp} and Z coefficients α and b, the attenuation in the horizontal channel A_h can be written as

$$A_h = \alpha K_{dp}^b \tag{2.20}$$

Since precipitations cause radar signals to scatter and be absorbed, the measured Z calculated by the signals received by the radar can be lower than intrinsic Z [15]. To account for the difference present in the Z datasets, the attenuation can be described in terms of the phase delays caused by the rain media at each range location [7]. Therefore, the measured Z, written as Z_m, and the intrinsic Z written as Z can be written as

$$Z_m(r) = Z(r) - 2\int_0^r A(S)dS \tag{2.21}$$

The attenuation coefficient A can be replaced by K_{dp} in combination with the Z coefficient α [15]. Therefore, assuming $b = 1$, Z_m and Z can be described as

$$Z_m(r) = Z(r) - 2\alpha\int_0^r K_{dp}(S)dS \tag{2.22}$$

ϕ_{dp} presents the accumulation of K_{dp} along the propagation path. Mathematically, ϕ_{DP} is the area under the curve of K_{dp}, and K_{dp} is the derivative of ϕ_{dp} [15]. Therefore, Z_m be described in terms of ϕ_{dp} as

$$Z_m(r) = Z(r) - 2\alpha[\phi_{dp}(r) - \phi_{dp}(0)] \quad (2.23)$$

The intrinsic Z can be written as

$$Z(r) = Z_m(r) + 2\alpha[\phi_{dp}(r) - \phi_{dp}(0)] \quad (2.24)$$

The coefficient α varies depending on the wavelength of the radar, temperature, and drop size distribution (DSD). DSD can be calculated using two methods: using the gamma distribution model and measurement from disdrometers. The value of α was computed for a variety of DSD, where the Gamma distribution model was used, and for a range of temperature from 0 to 30^oC. The scattering simulation was averaged and as a result, the value of α was reported to be 0.073 for a C-band radar [25]. In the RELAMPAGO campaign, disdrometers were deployed near CSAPR to measure DSD and scattering simulations were used to compute the DSD from November to December 2018 with a T-matrix procedure with a value of 10^oC for the temperature. As a result, the value of α during the RELMAPAGO campaign was calculated to be 0.15 [25].

2.3.3 Z_{dr} Bias Correction

Z_{dr} is a widely used radar product to indicate the shapes of raindrops. Z_{dr} data is collected by dual-polarization radars, which transmit and receive both vertical and horizontal signals [1]. Positive and negative Z_{dr} indicate oblate- and prolate-shaped raindrops. Practically, negative Z_{dr} from precipitation is occasionally observed in hails, however, it is not commonly observed in liquid raindrops. This is because liquid precipitations typically consist of perfectly

spherical and oblate-shaped raindrops, which correspond to 0 dB and positive values of Z_{dr}, respectively.

Z_{dr} bias occurs in almost all campaigns with meteorological radar systems due to a variety of reasons including bias occurring in radar hardware and signal processors. Although highly precise radar such as CHIVO radar presents very low Z_{dr} bias, it is critical to correct Z_{dr} to ensure high data quality. As it is limited to calibrating the hardware during radar operations, Z_{dr} is calibrated using software algorithms.

There are a few methods to calibrate Z_{dr}. One of the widely used methods to correct Z_{dr} is to collect light rain with the value of Z less than 20 dB and suppose that the value of Z_{dr} is 0 dB. This method is very basic yet powerful because light rain precipitation consists of raindrops in perfectly spherical shapes. According to [28], the authors argue that Z_{dr} = 0 dB at Z = 20 dB is around 0.23 dB with standard deviation of 0.2 dB. For this reason, assuming raindrops to be perfectly spherical in this scenario is valid. Using this theory, light precipitation below the melting layer can be collected using vertical-pointing 360-degree PPI scans and the data can be used to obtain Z_{dr} bias. In this case, two methods can be used to evaluate the data: Z_{dr} versus Z dispersion analysis and histogram analysis. If the quality of the collected data is above the threshold, the mean and median of the data can be obtained, which provides information on Z_{DR} bias. The second way to correct Z_{dr} bias is to use the sun as a reference. By simultaneously sending test signals to the sun, the gain in the active and passive parts of transmitting and receive paths can be monitored to obtain Z_{dr} bias [29]. The third way to calibrate Z_{dr} is to use the cross-polar power approach. Theoretically, returned power signals from fixed targets, which can be obtained by sending fast alternating horizontal and vertical signals are equal. For the cross-power approach, simultaneous signals can be sent to ground targets at low-elevation angles [29]. This

method considers the fact that the radar scattering matrix S_{hv} and S_{vh} are equal, therefore, Z_{DR} bias can be obtained by comparing the average cross-polar powers at vertical and horizontal polarizations, which can be presented as

$$Z_{dr}^{cal} = Z_{dr}^{m} S^2 \frac{P_{xv}}{P_{xh}} \tag{2.25}$$

Where Z_{dr}^{cal} is to-be calibrated Z_{dr}, Z_{dr}^{m} is measured Z_{dr}, S is a scattering matrix, and P_{xv} and P_{xh} are average cross-polar powers at vertical and horizontal polarizations respectively.

When there is insufficient precipitation data from vertical-pointing scans, the sun can be used as a reference to obtain Z_{dr} bias [29]. When the sun is used as a reference, vertical and horizontal co-polar and cross-polar sun radiation can be observed to obtain Z_{dr} bias as

$$Z_{dr}^{cal} = Z_{dr}^{m} S_{copolar} S_{crosspolar} \frac{P_{xv}}{P_{xh}} \tag{2.26}$$

Where $S_{copolar}$ is the ratio of vertical to horizontal-co polar sun radiation, and $S_{crosspolar}$ is the ratio of vertical cross-polar to horizontal cross-polar sun radiation.

Depending on weather conditions and scanning strategies, a method can be chosen to correct Z_{dr} bias. For example, on precipitation-free days, the best reference to obtain Z_{dr} bias is the sun. On the other hand, in the case of frequent precipitation throughout the campaign, light rain precipitation below the melting layers is the best reference. During the RELAMPAGO campaign, CHIVO radar collected abundant light precipitation data using vertical-pointing PPI scans. For this reason, light precipitation data were chosen to be the best reference for the campaign.

2.3.4 Relative Calibration Adjustment (RCA)

The Z data collected by radar is prone to fluctuations due to changes in power, elevation angle, and attenuations caused by precipitation events [30]. There are many ways to calibrate Z

using precipitation data including the self-consistency principle, however, applying the self-consistency principle to obtain Z bias requires ideal precipitation events, which are not easily observed. To address this issue, Relative Calibration Adjustment (RCA) can be used to observe fluctuations in Z from fixed ground targets such as mountains and buildings. For this reason, RCA is particularly useful for cases, in which little or no precipitation is present. During the RELAMPAGO campaign, only a few precipitation events were determined to be appropriate for applying the self-consistency principle. This is because heavy precipitation events and precipitation-free days were common during the campaign. Therefore, RCA was used to observe fluctuations in Z from the ground targets on precipitation-free days. More specifically, RCA was applied to obtain the mean and median of Z from ground targets for every precipitation-free day to produce valuable insights into fluctuations in Z. As the name "relative" suggests, RCA does not calculate absolute Z bias. Instead, results from RCA show changes in Z for ground targets within the 5-km range for each selected time window. Since precipitation significantly degrades the accuracy of RCA due to attenuations being present along propagation paths between radars and the selected ground targets, only precipitation-free days were selected to apply RCA to obtain relative Z bias.

2.3.5 Self-Consistency principle

The theory of the self-consistency principle asserts that measured Z, Z_{dr}, and K_{dp} within rain media lie in a 3-dimensional space. In other words, the three variables, Z, Z_{dr}, and K_{dp} are co-related [31]. Given two of the three variables, the other variable can be calculated using the self-consistency principle. The self-consistency principle has been widely used for a variety of applications including hail detections and Z bias correction. In this thesis, the self-consistency principle is used to obtain Z bias from light rain media. It is important to note that K_{dp}, ϕ_{dp}, Z,

and Z_{dr} are correlated only if an ideal light rain medium is used. Furthermore, there must be no precipitation present over the radar dome, which could cause significant attenuation, therefore, producing incorrect results. For this reason, ideal rain cells with Z less than $25\ dB$ must be carefully collected and used.

An important role of self-consistency is obtaining absolute Z bias, which can be used as a reference; the self-consistency principle obtains the absolute Z bias from light rain cells to be compared to the results obtained by RCA. To apply the self-consistency principle, ideal rain cell data first had to be identified. Figure 2.6 shows ideal rain cell characteristics in terms of Z, ϕ_{dp}, and K_{dp}. It is important to note that the data must not include hail or melting layers to obtain accurate results. Z within the range (r_0, r_m) along the ideal rain cell shows increasing and decreasing characteristics for an ideal light rain medium. Due to the path attenuation within the range (r_0, r_m), phase delays occur along the path, therefore, range-dependent ϕ_{dp} steadily increases from $r_0\ to\ r_m$.

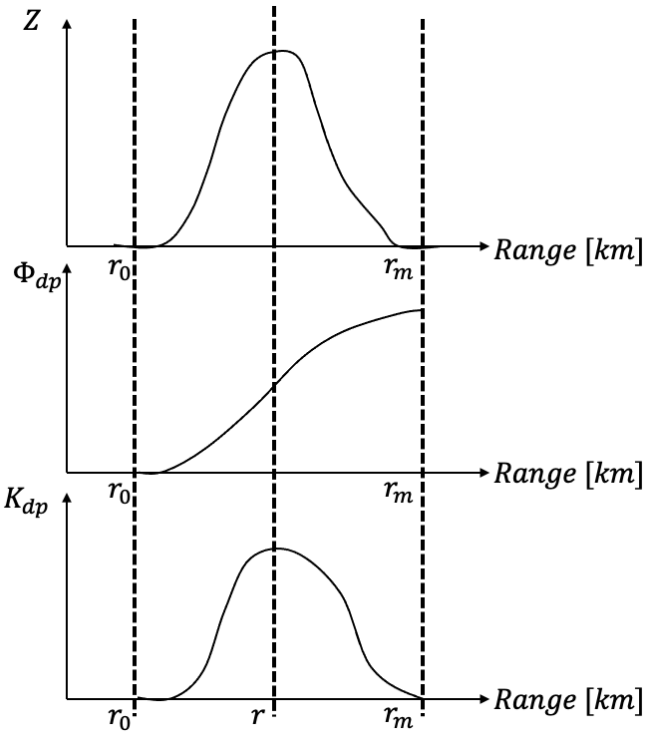

Figure 2.6: Ideal rain cell characteristics identified by $Z, \phi_{dp},$ and K_{dp}.

As electromagnetic waves pass through the rain medium along the propagation path, the waves slow down. This is caused by propagation delays when the waves pass through the medium, therefore, phase shifts can be observed. For dual-polarization radars, propagation delays at horizontal and vertical polarizations can be observed. Utilizing phase shifts at vertical and horizontal polarizations, K_{dp} and ϕ_{dp} can be derived to obtain more information: how many oblate and larger raindrops are present within the given rain medium. From ϕ_{dp}, which indicates cumulative phase shift along the propagation path, K_{dp}, which indicates the difference in phase shift between horizontal and vertical polarizations at each range location can be derived. Unlike Z_{dr}, which presents the number of large and oblate raindrops, K_{dp} indicates the density of raindrops in the rain medium, which provides details on the characteristics of the precipitation. Ranging from -2 to 7 deg/km, positive K_{dp} indicates that a high density of oblate-shaped raindrops, which are relatively large sizes are present in the rain medium [21]. Since K_{dp}

indicates the ratio of phase shift at horizontal to vertical polarization, forward scatter amplitudes at horizontal and vertical polarizations are used to calculate K_{dp} as

$$K_{dp} = \frac{180}{\pi} \lambda Re[\int_{D_{min}}^{D_{max}} [f_h(D) - f_v(D)]N(D)dD \ [degkm^{-1}]] \quad (2.27)$$

Where λ is the radar wavelength, $f_h(D)$ and $f_v(D)$ are forward scattering amplitudes at horizontal and vertical polarizations, respectively, and $N(D)$ is DSD.

To apply the self-consistency principle to obtain Z bias, ϕ_{dp}, which indicates the cumulative phase shift along the propagation path, can be reconstructed from the calculated K_{dp} [21]. ϕ_{dp} can be expressed as an accumulation of K_{dp} along the propagation path. Therefore, ϕ_{dp} can be described as

$$\phi_{dp} = 2\int_{r_0}^{r} K_{dp}(s)ds \quad (2.28)$$

Due to the scattering and absorption of electromagnetic waves in the rain medium, backscattering propagation is observed when the waves return to the radar [1]. For this reason, the phase difference caused by backscattering propagation must be considered [20]. Considering the backscattering propagation, ϕ_{dp} can be calculated as

$$\phi_{dp} = \varphi_{dp} + \delta \quad (2.29)$$

Where δ is the phase difference due to the backscattering propagation.

Since K_{dp}, Z, and Z_{dr} are correlated within a 3-D space, K_{dp} can be calculated using Z and Z_{dr} in combination with coefficients, which depend on the radar parameters. Referring to [32], K_{dp} can be expressed as

$$K_{dp} = CZ_h^{\alpha}10^{-\beta Z_{dr}} \quad (2.30)$$

Where the coefficients depend on the wavelength of the radar. For C-band (5.5 cm) CSU CHIVO radar, the coefficients are: $C = 1.4610^{-4}, \alpha = 0.98, and\ \beta = 0.2$.

Z can be expressed in terms of Z_{dr} and K_{dp} in combination with the coefficients C, α, and β [32] as

$$Z = (\frac{1}{C}\frac{K_{dp}}{10^{-\beta Z_{dr}}})^{1/\alpha} \tag{2.31}$$

Similarly, Z_{dr} can be expressed in terms of Z and K_{dp} in combination with the coefficients C, α, and β [32] as

$$Z_{dr} = \frac{1}{\beta}(log_{10}C + log_{10}K_{dp} - \frac{\alpha}{10}10log_{10}Z) \tag{2.32}$$

The Z bias can be also obtained by comparing the measured K_{dp} and constructed K_{dp} [32] as

$$\delta Z(dB) = \frac{10}{b} log_{10}(\frac{K_{dp_m}}{K_{dp_c}}) \tag{2.33}$$

Where δZ is Z bias in dB, K_{dp_c} and K_{dp_m} are constructed and measured K_{dp}, respectively.

After K_{dp} is constructed from Z and Z_{dr}, ϕ_{dp} can be constructed in terms of K_{dp} [32] as

$$\phi_{dp}(r) = \sum_{r_o}^{r} K_{dp}(r)\Delta r + constant \tag{2.34}$$

Where the constant indicates the phase shift along the propagation path where the rain cell starts to be present.

To evaluate the difference between the constructed and measured ϕ_{dp}, the bias can be obtained as

$$\phi_{dp}\ Bias = \sum \phi_{dp_c}(r) - \phi_{dp_m}(r) \tag{2.35}$$

Where ϕ_{dp_c} and ϕ_{dp_m} are constructed and measured ϕ_{dp}, respectively.

2.4 CSU CHIVO Radar Calibration

Using the data collected by CHIVO radar, many research projects have been conducted to understand a variety of weather phenomena. The ongoing projects include finding the connection between convection, severe weather development, complex terrains, and soil characteristics. By better understanding the weather phenomena, researchers will be able to provide innovative solutions to improve weather prediction models and weather warning systems. Ultimately, by improving weather-related prediction models, the projects will significantly contribute to improving natural disaster warning systems, which will reduce infrastructural and agricultural damages, and casualties, which are caused by powerful natural disasters today. As shown in Figure 2.7, CHIVO radar was deployed south of Córdoba, Argentina, nearby Alta Gracia, and Rio Secundo.

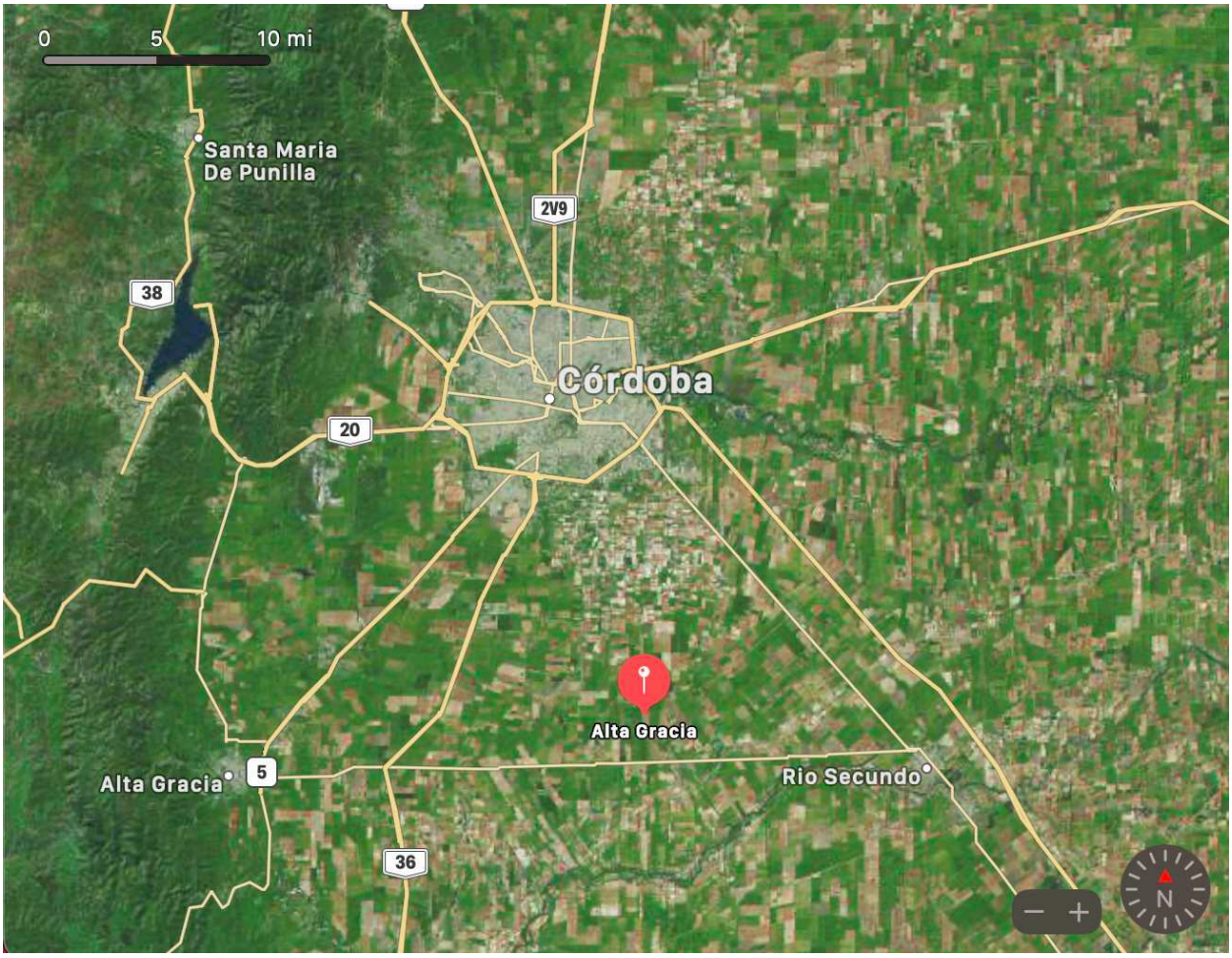

Figure 2.7: Location of CHIVO deployment during the RELAMPAGO campaign.

The main objectives within the context of CHIVO radar calibration were to correct azimuth, Z, and Z_{dr} after the campaign using the following calibration techniques: azimuth correction, Z_{dr} bias correction, attenuation correction, and Z bias correction using RCA and the self-consistency principle. Although weather radars can be calibrated using hardware-based approaches, they hinder radar operations significantly. For example, when precipitation is present while the radar is being calibrated, the radar misses an opportunity to collect valuable data from the precipitation. For this reason, the software-based calibration approaches mentioned above were used and are presented in this thesis.

The first step before obtaining Z bias was to correct the attenuation. This was because the attenuation correction and the ground filters in the data signal processor were intentionally turned off during the RELAMPAGO campaign. The reason the ground filters were turned off was that it was a good practice to collect raw data to obtain as much information as possible and handle the data to achieve the main objectives of the campaign using the software-based techniques possible. Within the context of calibration, attenuation correction was completed using the Z-PHI algorithm as presented in this thesis.

Since it was more difficult to obtain the absolute Z bias than the relative Z bias, most Z biases were calculated using RCA, and the absolute Z biases obtained by the self-consistency principle were used as references. RCA and the self-consistency principle supported each other's weaknesses with their strengths. The main strength of RCA was being able to collect ground target data, obtain mean and median Z, and observe changes in Z over time. In other words, the ideal weather condition under which RCA performed the best was precipitation-free. Applying RCA to obtain Z bias produced poor results when precipitation was present because precipitation caused significant attenuation on the radar signals. This was observed by applying RCA to precipitation-heavy cases, therefore, the cases with poor results produced by RCA due to precipitations were removed. In contrast, self-consistency required the ideal condition, under which the attenuation would affect the performance of RCA. For this reason, to obtain accurate Z bias for each case, RCA and the self-consistency principle were applied to cases without precipitation and with light precipitation, respectively.

Combining all these calibration methods, Z, Z_{dr}, and azimuthal data were corrected. To apply all radar calibration algorithms presented in this thesis successfully, correct procedures were taken to apply each calibration algorithm. First, attenuation correction was completed using

the Z-PHI method before any of the calibration techniques were applied because it would produce a significant error. Solar ray positions were collected using 3-degree PPI scans, azimuth errors were obtained by comparing the azimuth values obtained from NOAA Solar Position Calculator, and the azimuth errors were corrected for the entire RELAMPAGO campaign. After the azimuth correction was completed, the relative Z biases were obtained by applying RCA to the ground targets within 5 km. After RCA obtained relative Z biases, the absolute Z biases were obtained by applying the self-consistency principle using precipitation data with Z below 25 dBZ. When all the calibration techniques were combined, Z and Z_{dr} biases were obtained throughout the RELAMPAGO campaign. Figure 2.8 shows an appropriate set of procedures that were taken to combine the radar calibration techniques presented in this thesis.

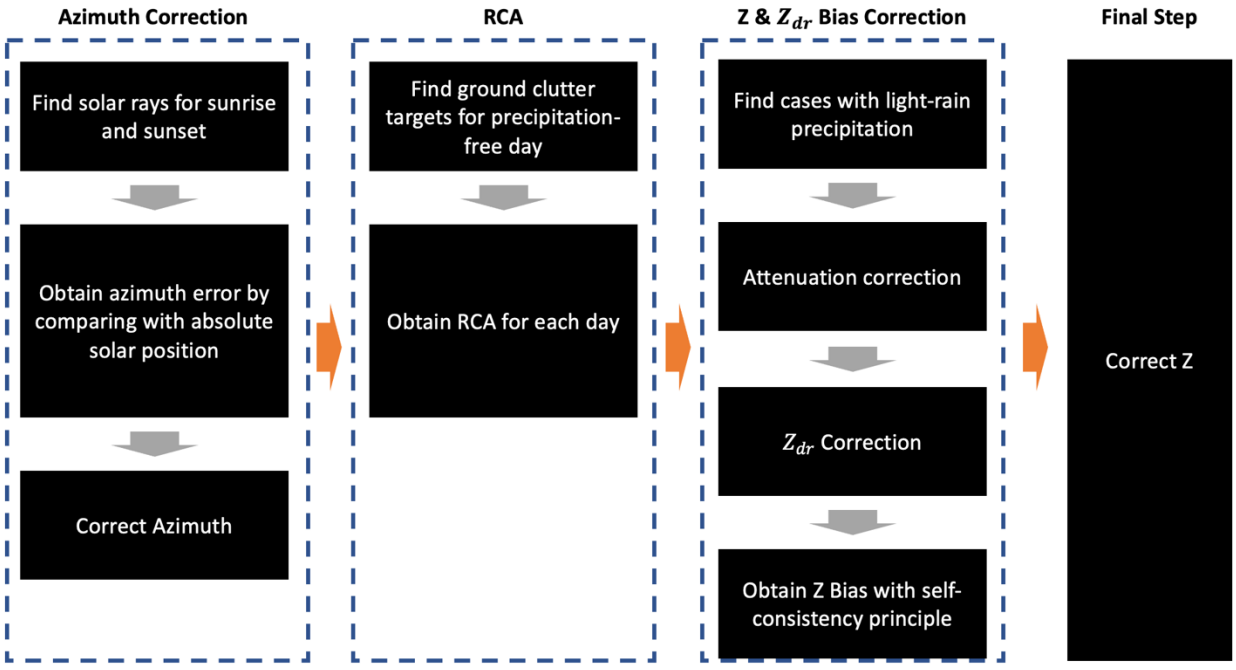

Figure 2.8: Radar calibration techniques presented in this thesis and their appropriate steps to correct Z and Z_{dr}.

Chapter 3

Azimuth Correction

3.1 Introduction

Azimuth correction was completed by comparing solar ray positions obtained by CHIVO radar and the absolute solar ray position, which was provided by NOAA Solar Position Calculator. Azimuth correction was critical to improving the performance of RCA, which depends on azimuth-dependent fixed ground targets. To correct the azimuth readings from CHIVO radar, the following methods were used to calculate the azimuth errors: 1) comparing an azimuth reading on a solar position from the radar and the absolute solar position at the location and the time using the positions from NOAA Solar Position Calculator as references, 2) tracking the motion of detected RF rays present during the partial or the entire day, and 3) tracking the positions of fixed ground targets, such as buildings at specific locations. Using the solar ray as a reference was reliable because it enabled obtaining the absolute azimuth error, however, locating the accurate position of the solar ray from the radar was limited because precipitation would cover the rays rendering the rays undetectable. Furthermore, the solar rays would be detected only two times a day at sunrise and sunset. On the other hand, some RF rays were present continuously for a few days or several weeks, therefore, azimuth errors could be calculated more frequently. Combining the absolute and relative azimuth errors calculated by referencing the position of solar and RF rays in combination with ground targets, azimuth errors were calculated continuously during the RELAMPAGO campaign.

3.2 Correction Algorithm Descriptions

The key to azimuth correction was to correct CHIVO radar's azimuth readings by using solar rays as references provided that CHIVO radar detected solar rays. Applying this method had a few constraints. First, for the solar rays to be detected by CHIVO radar at the sunset and/or the sunrise, there must be no significant precipitation present nearby the absolute solar ray positions. This was because radar signals returned from solar rays were significantly weaker than signals returned from typical precipitation, therefore, when precipitation was present nearby the rays, the solar rays were not identified. Second, at the time when solar rays were detected by the radar, the radar must be operating continuously. Ideally, the radar would be continuously scanning 360 degrees horizontally at the elevation angles between 0.5 to 90 degrees and vertically at the azimuths between 0 and 360 degrees. When the solar rays were detected by CHIVO radar, 3-degree PPI scans were used to identify rough solar ray positions at sunrise and sunset. When the solar ray positions were identified, plots on Z versus range were analyzed to locate the accurate positions of solar rays with an accuracy of ± 1 degree. When the exact azimuthal locations of the solar rays were identified, the absolute solar ray positions obtained by NOAA Solar Position Calculator were used to correct CHIVO azimuth readings. The final azimuth errors were obtained by subtracting the absolute positions of the solar ray from the radar azimuth readings.

Furthermore, positions of radio frequency (RF) rays and ground targets were tracked and recorded to observe the continuously changing positions of the targets each day. The main advantage of this method was to create azimuth data sets with high resolution. The relative azimuth data sets created by observing the RF rays and the ground targets were converted into the absolute azimuth bias by using the absolute azimuth biases obtained by the absolute solar ray

positions as references. Figure 3.1 shows a set of diagrams, which describe the procedures taken to correct azimuth biases during the RELAMPAGO campaign.

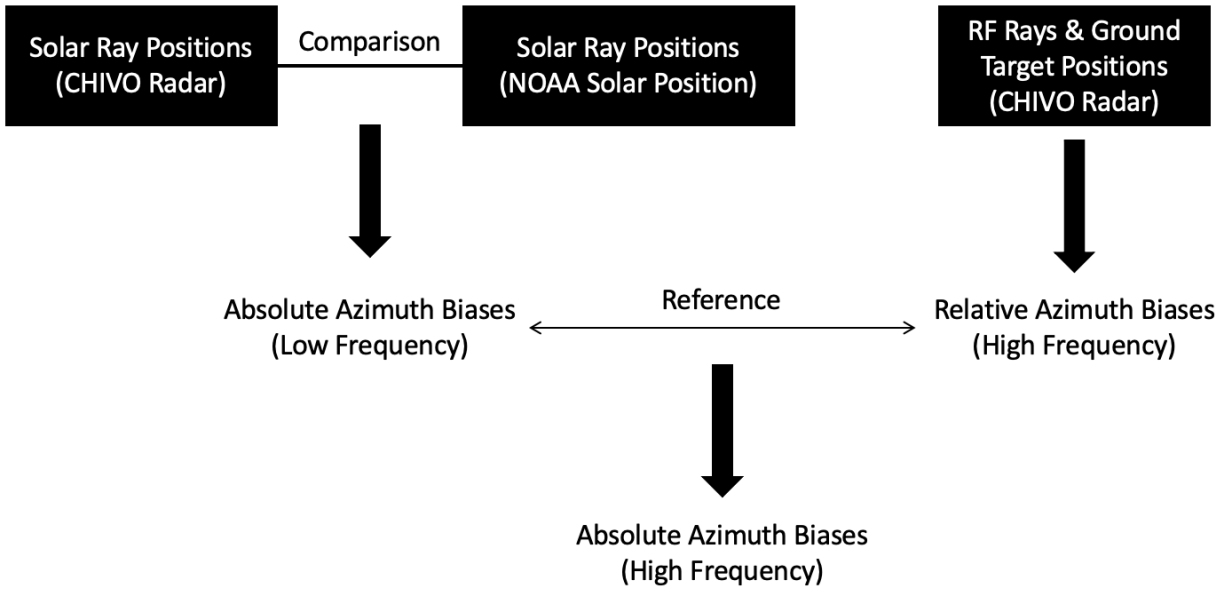

Figure 3.1: Diagrams, which describe the procedures taken to correct the azimuth biases using absolute azimuth bias obtained by the solar rays and relative azimuth biases obtained by tracking RF rays and ground targets.

3.3 Results

Figure 3.2 shows solar rays detected by 0.5-degree PPI scans on December 29, 2018, and December 31, 2018, where the detected solar rays are marked with red circles. For both cases, CHIVO radar detected the solar rays at 9:20 AM UTC. As shown in the figure, solar rays along with other unknown rays were observed. To verify the rays, NOAA Solar Position Calculator was used to determine the expected position and time at which the solar rays would be present. In these cases, the solar rays were expected to be located near the 115-degree azimuth.

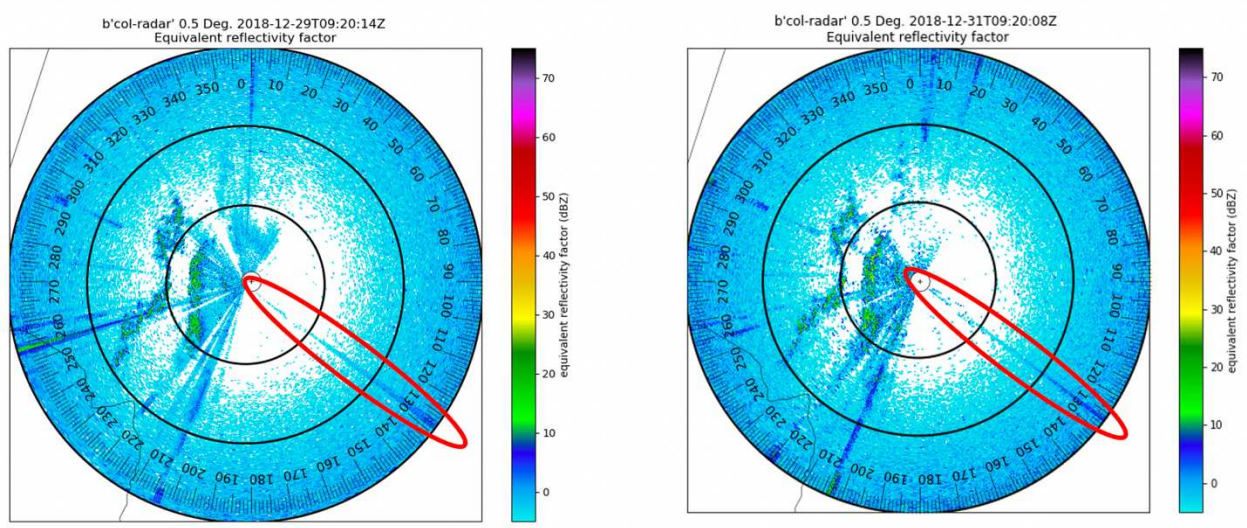

Figure 3.2: Two solar ray cases identified by 0.5-degree PPI scans, which are marked with the red circles for 12/29/2018 (left) and 12/31/2018 (right).

Figure 3.3 shows an example of obtaining absolute solar ray position from NOAA Solar Position Calculator, which corresponds to a ray observed by a 3.3-degree PPI plot on 12/28/2018 at 09:31:52 UTC. NOAA Solar Position calculator provided details on solar positions when the time and the location of the radar were provided. Useful information in the context of azimuth correction includes an elevation angle of a solar position and an expected azimuthal location of the solar ray. Since CHIVO radar conducted PPI scans continuously at varying elevation angles from 0.5 to 90 degrees, the radar detected solar rays successfully.

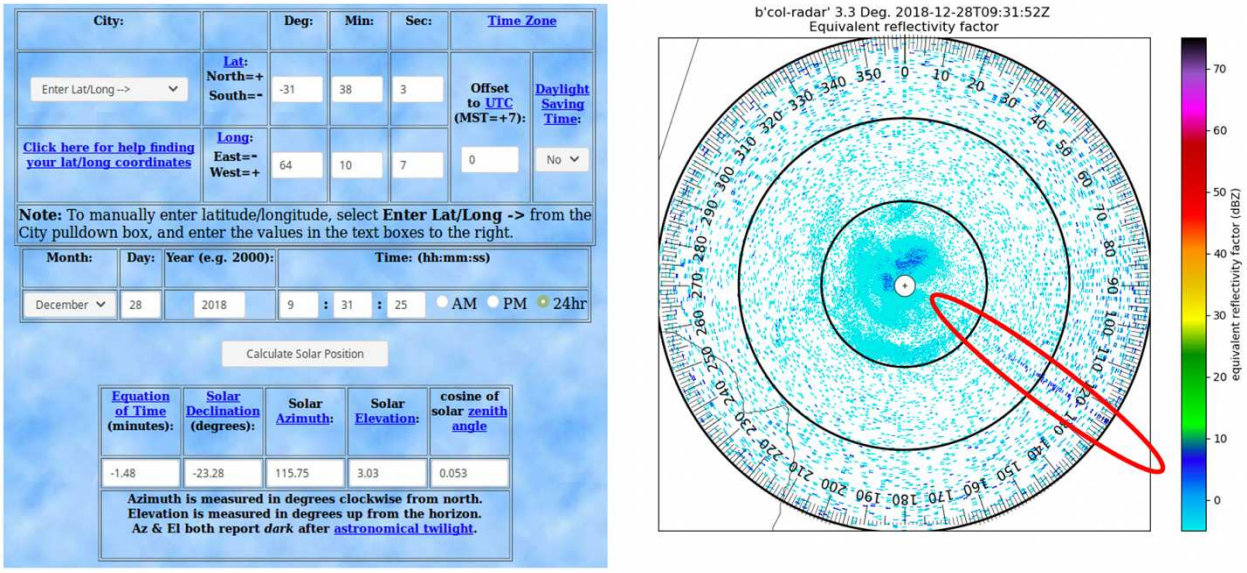

Figure 3.3: Example of locating the absolute solar position using NOAA Solar Position Calculator and comparing its azimuth with CHIVO radar's azimuth reading on the solar ray.

Figure 3.4 shows Z versus range plots for a detected solar ray at 0.5- and 1.46-degree elevation angles. As shown in the plots, Z increases from 0 to approximately 5 dB from 80 to 150 km. These characteristics observed by the Z versus range plot were used as references to confirm the exact location of other solar rays. As these characteristics were also present for other RF rays, positions of other RF rays were tracked to observe azimuth changes throughout the day.

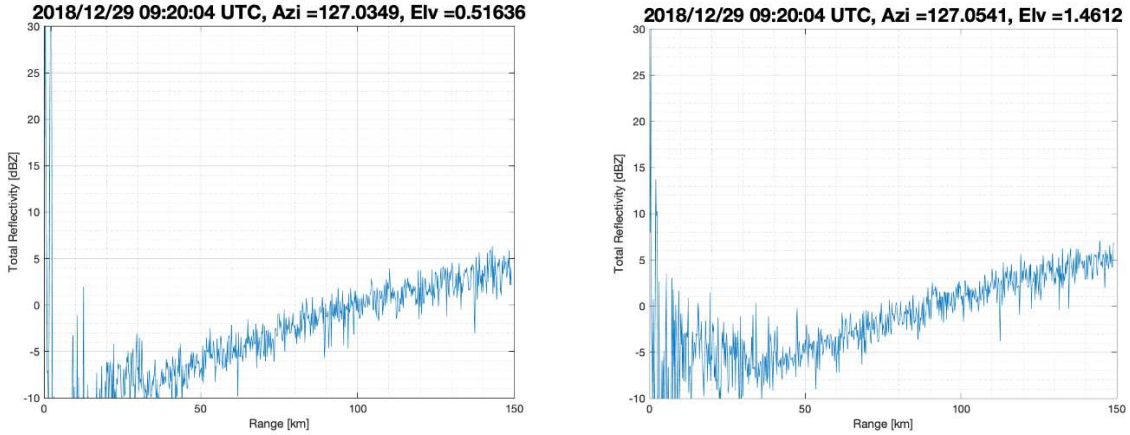

Figure 3.4: Total reflectivity characteristics of the solar rays shown by RHI scans, which were used to verify the locations of the rays.

Tracking and recording RF ray positions provided more information on how much the radar was drifting during each day, which allowed the observer to overcome the challenges associated with the limited availability of the solar rays. Figure 3.5 shows RF rays for two cases:

November 23, 2018, and December 22, 2018, where the azimuthal positions of the identical RF ray were 194 and 201.5 degrees, respectively.

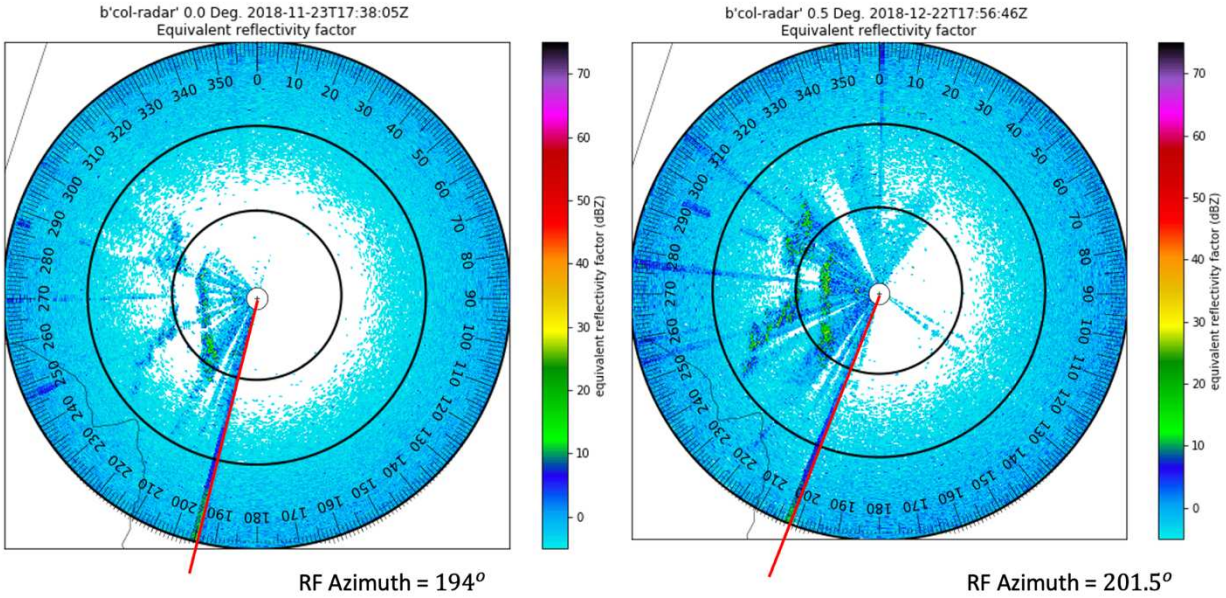

Figure 3.5: An identical RF ray detected by CHIVO radar (marked by red lines) on November 23, 2018 (left), and December 22, 2018 (right).

As CHIVO radar was continuously conducting PPI and RHI scans throughout the RELAMPAGO campaign, low-elevation (0.5-degrees) PPI scans collected ground targets. In the context of azimuth correction, continuously changing positions of fixed ground targets were used to calculate the relative azimuth biases. The ground targets typically returned the value of Z over 50 dBZ. Figure 3.6 shows an example of the ground targets, which were seen as "shifting" clockwise by CHIVO radar, as the radar was drifting counterclockwise during the campaign.

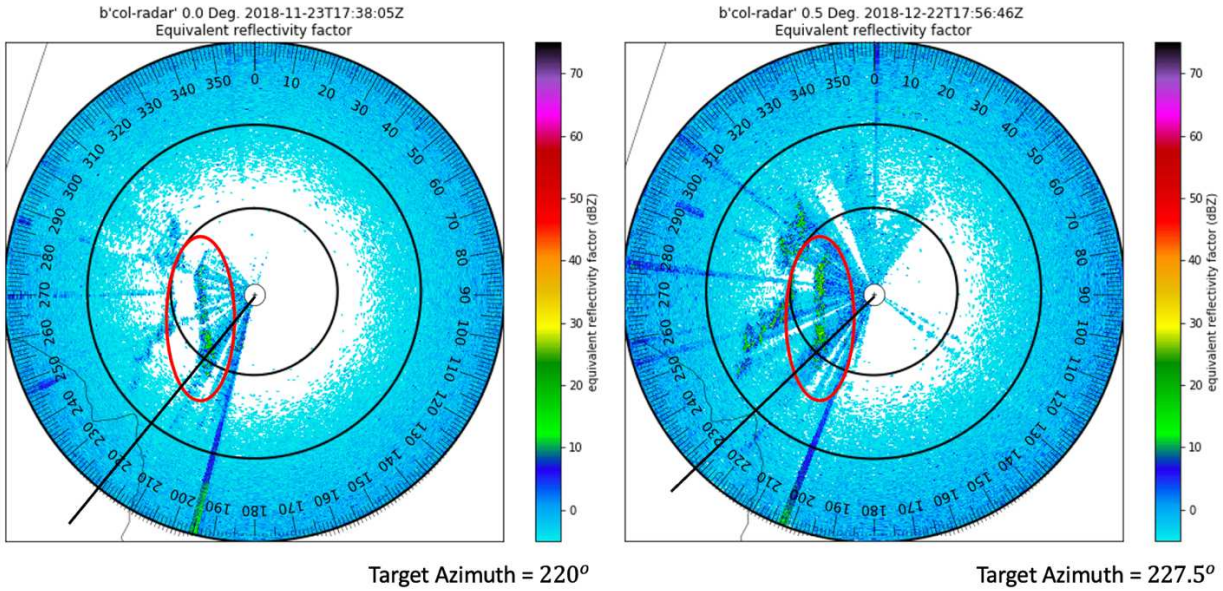

Figure 3.6: An identical ground target detected by CHIVO radar (marked by red circles, which indicate an area where the targets were present, and the black lines), which indicate the position of a sample ground target, where the target was detected at the azimuth of 220 and 227.5 degrees on November 23, 2018 (left), and December 22, 2018 (right), respectively.

Figure 3.7 shows azimuth drift calculated by subtracting absolute solar ray position from the solar ray position from CHIVO radar. Continuously increasing positive azimuth error suggests that the radar was drifting counterclockwise. The error bars indicate the standard deviation of the azimuth drift for each day, which was calculated by tracking the locations of RF rays and ground targets. As shown in the figure, the radar was drifting counterclockwise, starting from an azimuth error of 3 degrees on December 1, 2018, to above 12 degrees at the end of the operation.

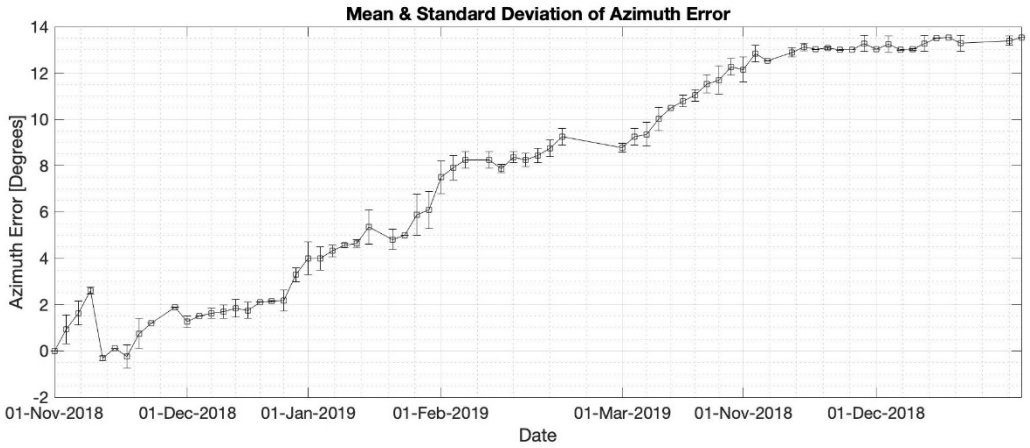

Figure 3.7: Azimuth errors for each day for CHIVO radar during the RELAMPAGO campaign, where the bars show the standard deviation of the azimuth error for each date.

3.4 Summary

The main objectives of correcting the azimuth errors were to improve the accuracy of the locations of the precipitations detected by CHIVO radar and to improve the performance of RCA, which utilizes location-dependent data from the ground targets. Within the context of the radar calibrations, the azimuth correction improved the performance of RCA significantly as presented in this thesis. Furthermore, observing the shift in the locations of the solar and RF rays as well as ground targets indicated that calibrating the horizontal location of the radars is crucial for radar operations for weather applications.

Chapter 4

Z_{dr} Bias Correction

4.1. Introduction

During the campaign, CHIVO radar was positioned at an approximately 90-degree elevation angle and rotated 360 degrees horizontally to collect raindrops to be used as references. If light raindrops were present, these raindrops seen from this vertical-pointing radar would be close to being perfectly spherical, which would return Z_{dr} close to 0 dB. Therefore, the mean and median Z_{dr} from these raindrops would indicate the errors present in the Z_{dr} measurement. For this reason, these raindrops were used to obtain the Z_{dr} bias. Since melting layers include ice crystals in a variety of shapes, the melting layer had to be avoided to collect light raindrops only. After removing the melting layers from the datasets, the datasets were evaluated by using vertical-pointing analysis and Z versus Z_{dr} dispersion analysis to verify that only light raindrops were collected. After the analysis, the final Z_{dr} bias was calculated and used as a reference to correct the Z_{dr} bias.

4.2 Correction Algorithm Descriptions

Z_{dr} bias correction for the RELAMPAGO campaign was completed by utilizing light precipitation data collected by CHIVO radar, which was collected while being positioned at the elevation angle of 90 degrees and being rotated 360 degrees horizontally. Light rain droplets seen vertically from the ground can be presumed to be in spherical shapes, therefore, Z_{dr} bias was obtained using this principle. Using the collected data, data quality evaluations were conducted based on histograms and Z_{dr} vs Z dispersion plots. To avoid melting layers, which

include ice crystals, the light precipitation data were carefully collected within 4 km from the ground. To further ensure collecting pure rain cells, the data were filtered by the following constraints: SNR > 10 dB, σ_{hv} > 0.95, Z < 20 dB. As a result, many bins were concentrated close to the actual Z_{dr} bias and a relatively small number of bins were spread out between +5 dB and –5dB. Figure 4.1 shows the entire procedure to analyze Z_{dr} data and correct Z_{dr} bias.

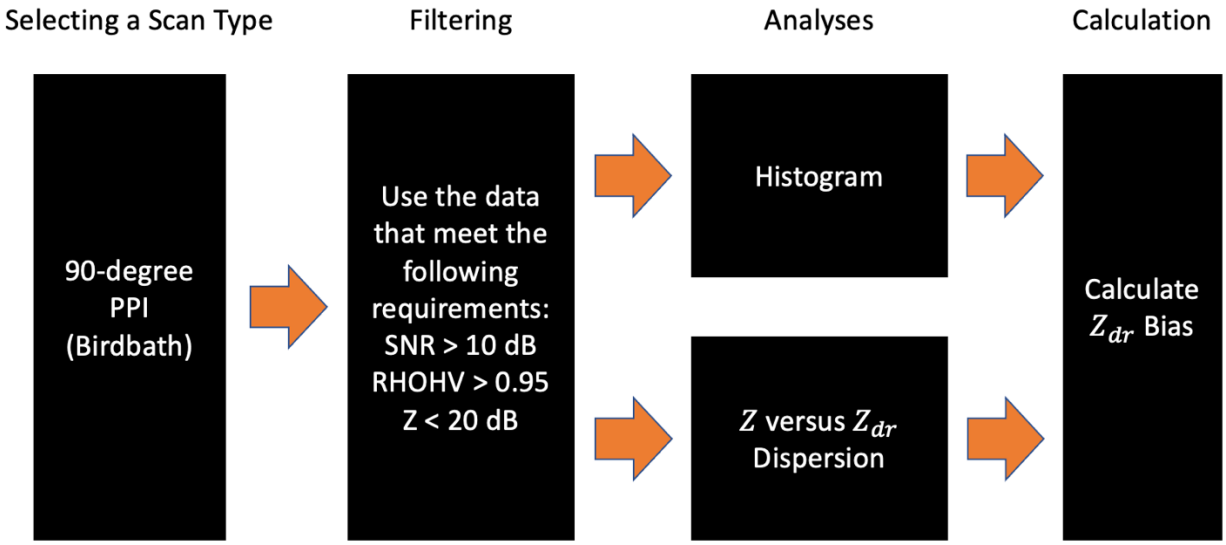

Figure 4.1: Appropriate steps taken to obtain Z_{dr} bias, where histograms and Z versus Z_{dr} dispersion analyses based on birdbath (90-degree) PPI scans were conducted to validate rain cells before calculating Z_{dr} bias.

4.3 Results

Figure 4.2 shows two 0.5-degree PPI plots for light-precipitation cases on January 3, 2019, and January 26, 2019. As shown in the figure, light precipitation was present with a value of Z approximately between 10 and 20 dB.

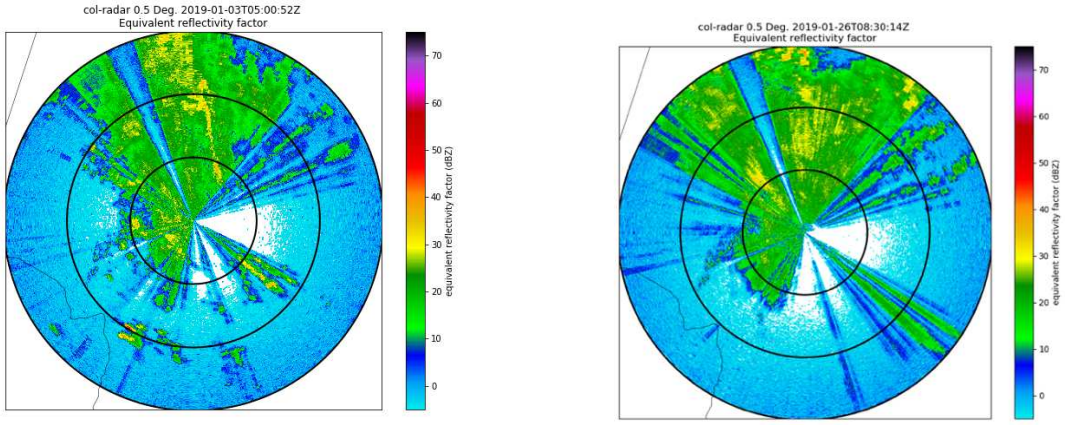

Figure 4.2: Light rain event observed by 0.5-degree PPI plots during the RELAMPAGO campaign.

Figure 4.3 shows histograms on January 3, 2019, and January 26, 2019, which were collected by CHIVO radar while being pointed vertically and rotated 360 degrees horizontally. Figure 4.4 dispersion analyses for the two cases, which show the mean and standard deviation of Z_{dr} for the Z data points between 10 and 35 dB.

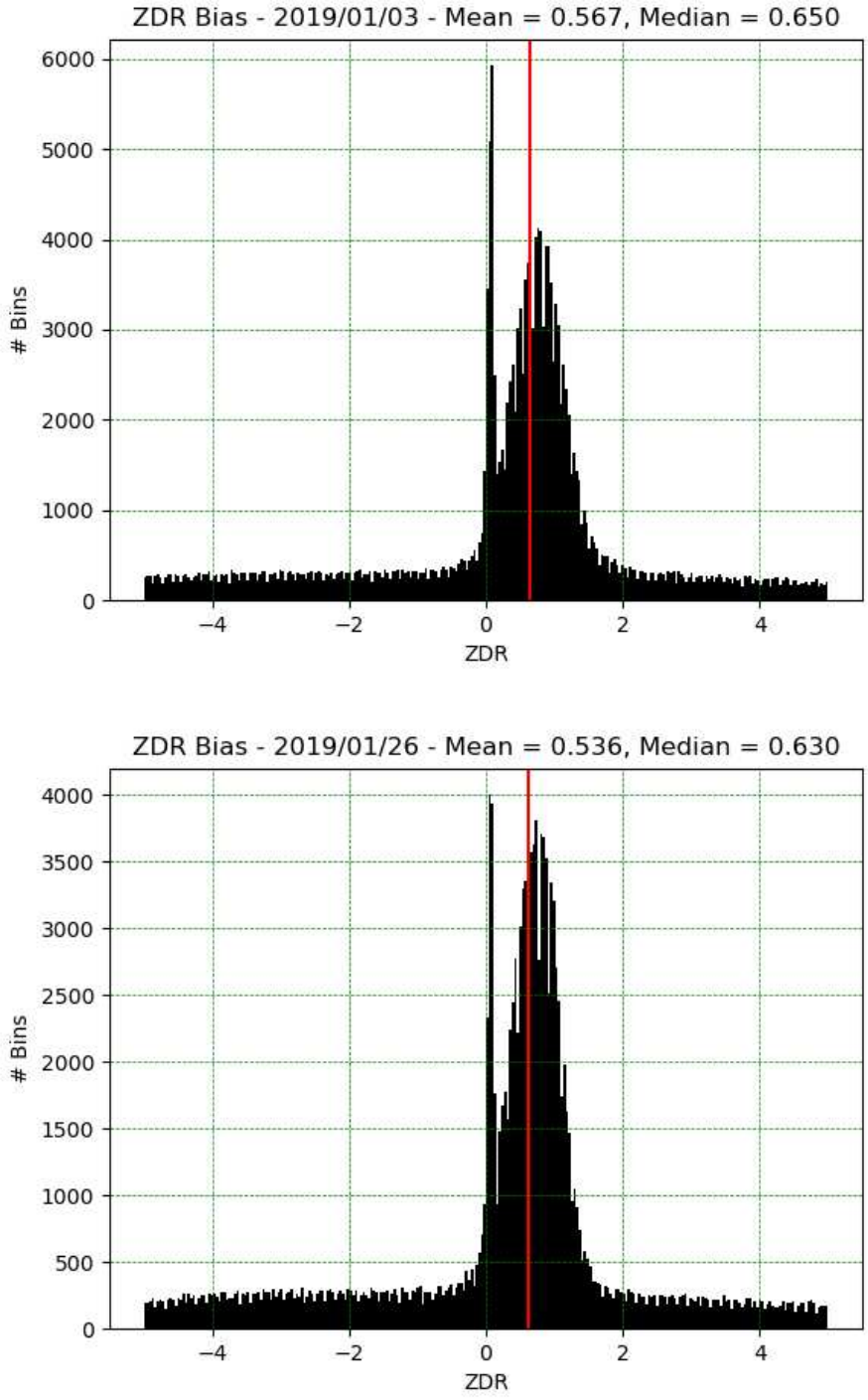

Figure 4.3: Histograms, which show Z_{dr} distribution of light rain data collected by birdbath (90-degree horizontal) scans during the RELAMPAGO campaign.

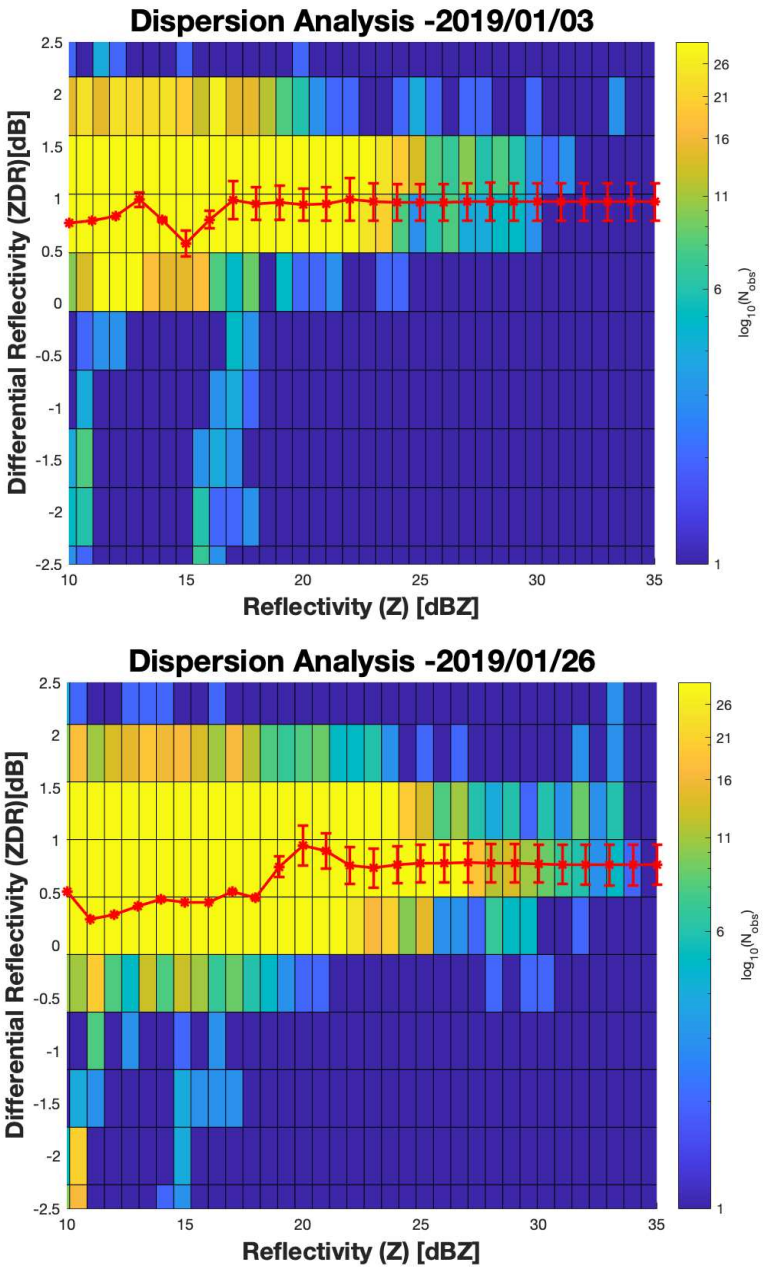

Figure 4.4: Z_{dr} and the corresponding Z data for distributions, where the red dots indicate the mean of Z and the bars indicate the standard deviation of the Z_{dr} data points along the corresponding Z from 10 to 35 dBZ. For these dispersion analyses, data obtained by birdbath (90-degree) PPI scans were utilized.

Table 4.1: Mean and Median of Z_{dr} bias for the RELAMPAGO Campaign

January 3, 2019		**January 26, 2019**	
Mean	Median	Mean	Median
0.567 [dB]	0.65 [dB]	0.536 [dB]	0.630 [dB]

4.3 Summary

Among many other methods to correct the Z_{dr} bias, the Z_{dr} bias correction method using the light raindrops seen vertically from the radar proved to produce the most reliable results. The high performance of this Z_{dr} bias correction method was demonstrated by verifying the pure rain cell characteristics with a low standard deviation of Z_{dr} between the value of Z ranging from 10 and 35 dBZ. Furthermore, it was demonstrated that the histograms of the Z_{dr} from the vertical-pointing scans were crucial to verify the light rain cell characteristics, which are expected to contain the data points near the Z_{dr} of 0 dB.

As Z_{dr} provides the shapes of raindrops, Z_{dr} bias correction is a crucial component to ensure high radar data quality. The key to Z_{dr} bias correction was identifying the right light rain cells as targets, calculating Z_{dr} bias from the correct datasets, and verifying the results by using the analysis methods presented in this chapter.

Chapter 5

Relative Calibration Adjustment (RCA)

5.1 Introduction

During the RELAMPAGO campaign, CHIVO radar was operating continuously regardless of precipitation events using PPI and RHI scans at varying azimuths and elevation angles. As a result, the radar collected ground targets such as trees and buildings from 360-degree PPI scans at the elevation angle of 0.5-degrees. Z data above 50 dBZ were typically present over the areas, where the ground targets were located. For each precipitation-free day, the Z data from the ground targets were filtered out using histograms and cumulative distribution function (CDF) and analyzed to identify appropriate ground targets to obtain the relative Z bias. This method to calculate the relative Z bias is called RCA.

5.2 Algorithm Descriptions

The first step in RCA is to find ideal ground targets and analyze the data using the cumulative distribution function (CDF). CDF shows what values of Z are likely to be present in the area where the ground targets are located. Within the context of RCA, CDF is used to filter out undesired data points below the 95th percentile. In addition, histograms are analyzed to evaluate the data quality. In this step, the datasets would ideally consist of many data bins with Z above 50 dB. After high data quality is validated and undesired data points are filtered out, the final RCA can be calculated using Equation 5.1. In the equation, $RCA_{baseline}$ indicates mean Z in an ideal precipitation-free case, which can be used as a reference, to which other precipitation-free cases can be compared. In other words, RCA_{daily} can be obtained for each precipitation-free

case and compared to $RCA_{baseline}$. As the equation suggests, positive RCA indicates negative Z bias with respect to the selected baseline date because $RCA_{baseline}$ would be higher than RCA_{daily}.

$$RCA = RCA_{baseline} - RCA_{daily} \tag{5.1}$$

Where $RCA_{baseline}$ and RCA_{daily} are the mean Z of a selected reference case and another case to be compared, respectively.

Since the ground targets are tracked based on geographical locations, it is crucial to correct azimuth errors before RCA is applied. Furthermore, for RCA to be applied, the azimuth data must be standardized; the entire radar datasets must be moved from cartesian coordinates to polar coordinates with consistent azimuth values in matrix indices. The azimuth matrices were gridded from cartesian coordinates to polar coordinates using a CSU custom-developed program called "Radx2Grid".

Since setting a high maximum distance would degrade data quality due to the phase difference, ground targets were collected within a 5-km radius. Typically, ground targets return signals with high values of Z above 50 dBZ. For this reason, the minimum threshold of Z was set to 50 dBZ. According to [30], collecting ground targets with Z above 50 dBZ within 5 km would not be vulnerable to normal precipitation events. However, from several experiments, it was observed that RCA fluctuated significantly when precipitations were present. For this reason, RCA was only applied to precipitation-free cases to ensure robust results. In addition, the range resolution was converted from 0.2 km to 1 km as shown in Table 5.1 because the high range resolution of 0.2 km caused fluctuations in data points, which produced unreliable results. To flag ground targets consistently, if one of 5 pixels for each 1-km range returned over 50 dB, the corresponding one 1-km pixel, which consisted of the 5 pixels was flagged as ground targets, and

all the Z data within the 5 pixels were collected. Using this method, if targets were present at the same pixel location over 50% of the time on a selected day, the pixel that includes the targets was flagged.

Table 5.1: Range resolution conversion for RCA.

Original Resolution – CHIVO Radar (5 pixels each)	Converted Resolution (1 pixel each)
0.2, 0.4, 0.8, 1.0 km	1 km
1.2, 1.4, 1.6, 1.8, 2.0 km	2 km
2.2, 2.4, 2.6, 2.8, 3.0 km	3 km
3.2, 3.4, 3.6, 3.8, 4.0 km	4 km
4.2, 4.4, 4.6, 4.8, 5.0 km	5 km

5.3 Results

The fluctuations in Z throughout the RELAMPAGO campaign provided by RCA produced robust results. RCA provided useful information on changes in Z, which could be compared to the absolute Z bias obtained by GPM and by applying the self-consistency principle. After evaluations on precipitation events, there was no precipitation present on December 31, 2018, therefore, was selected as baseline date to be compared with other cases.

Figure 5.1 shows ground targets presented on a map within a 5-km radius on December 31, 2018. The color bar indicates how often the pixels were present during the day; being closer to red indicates that the ground targets were present close to 100% of the time during the day. On the other hand, being closer to green indicates that the targets were present close to 50% of the time during the day.

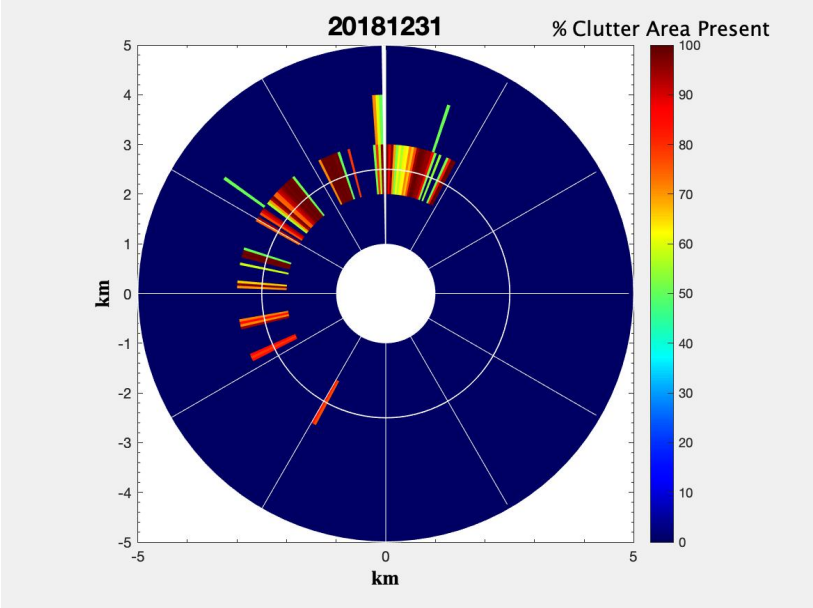

Figure 5.1: A clutter map, which shows for what percentage of the time during the day the ground targets were present at each location and was made by data collected by CHIVO radar on December 31, 2018, during the RELAMPAGO campaign.

Figure 5.2 shows a plot of cumulative distribution function (CDF) from the ground targets on December 31, 2018. CDF was used to filter out data with the minimum threshold of 95th percentile to utilize datasets that are highly likely to be the ground targets. In other words, using CDF allowed discarding data that were not likely to be the ideal targets before further analyses were conducted. Furthermore, as shown in Figure 5.3, histograms were plotted to evaluate the distribution of Z and verify the targets, where many data points above 50 dBZ were present for Z. After all these procedures were complete, the mean of Z was calculated for each date, which became the final value of RCA on that date.

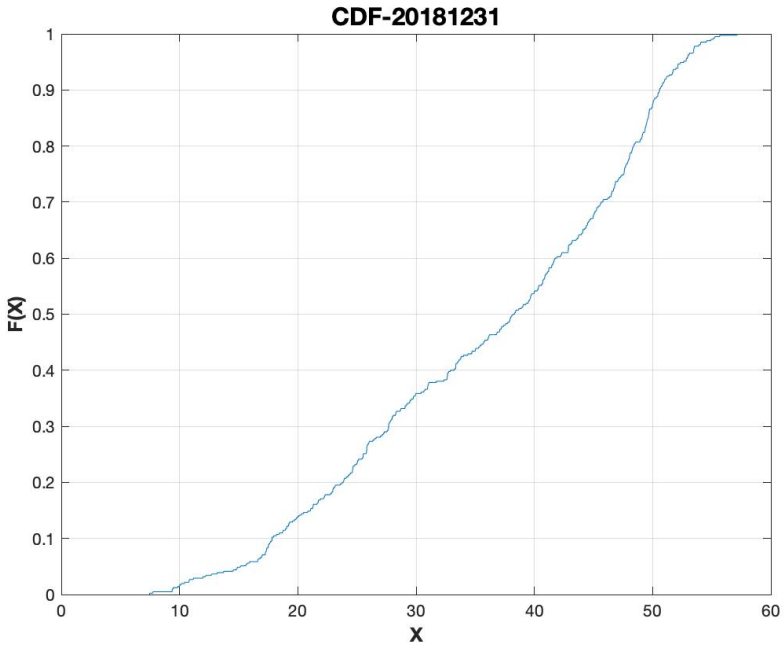

Figure 5.2: Cumulative Distribution Function (CDF) of the clutter data for December 31, 2018.

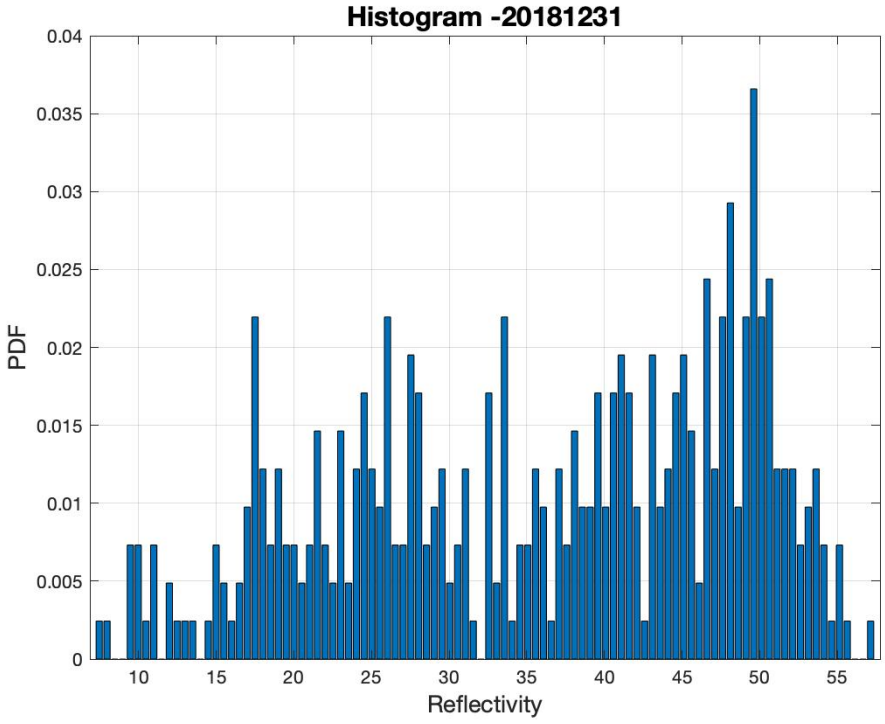

Figure 5.3: Histogram of the clutter data for the ground targets for December 31, 2018.

Using the same method, clutter maps were plotted for each precipitation-free case to be compared to the case on the baseline date. Figure 5.4 shows clutter maps for precipitation-free

days during the RELAMPAGO campaign. These cases were optimal for collecting and analyzing the ground targets, therefore, were used to obtain the mean and median of Z. It is important to note that correcting the azimuth reading of the radar significantly improved the confidence score of the clutter data points, therefore, improving the performance of RCA.

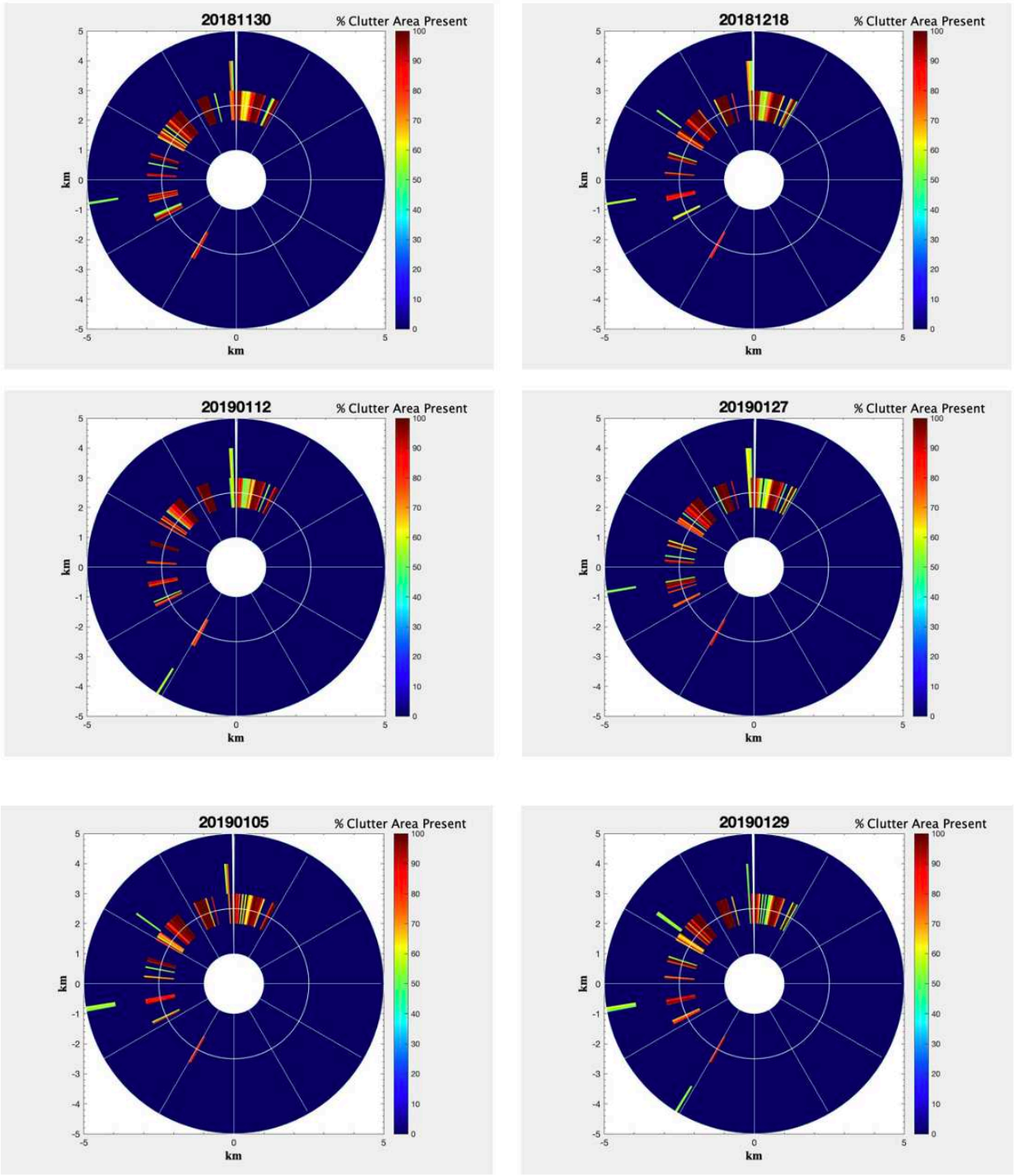

Figure 5.4: Clutter maps for the ground targets with azimuth correction.

Figure 5.5 shows CDF plots for each precipitation-free case, which were used to verify the ground targets. The characteristics of the CDF for each case demonstrate that Z data points

over 50 dBZ are highly likely to be the targets, therefore, verifying that the targets within the data sets are the ground targets.

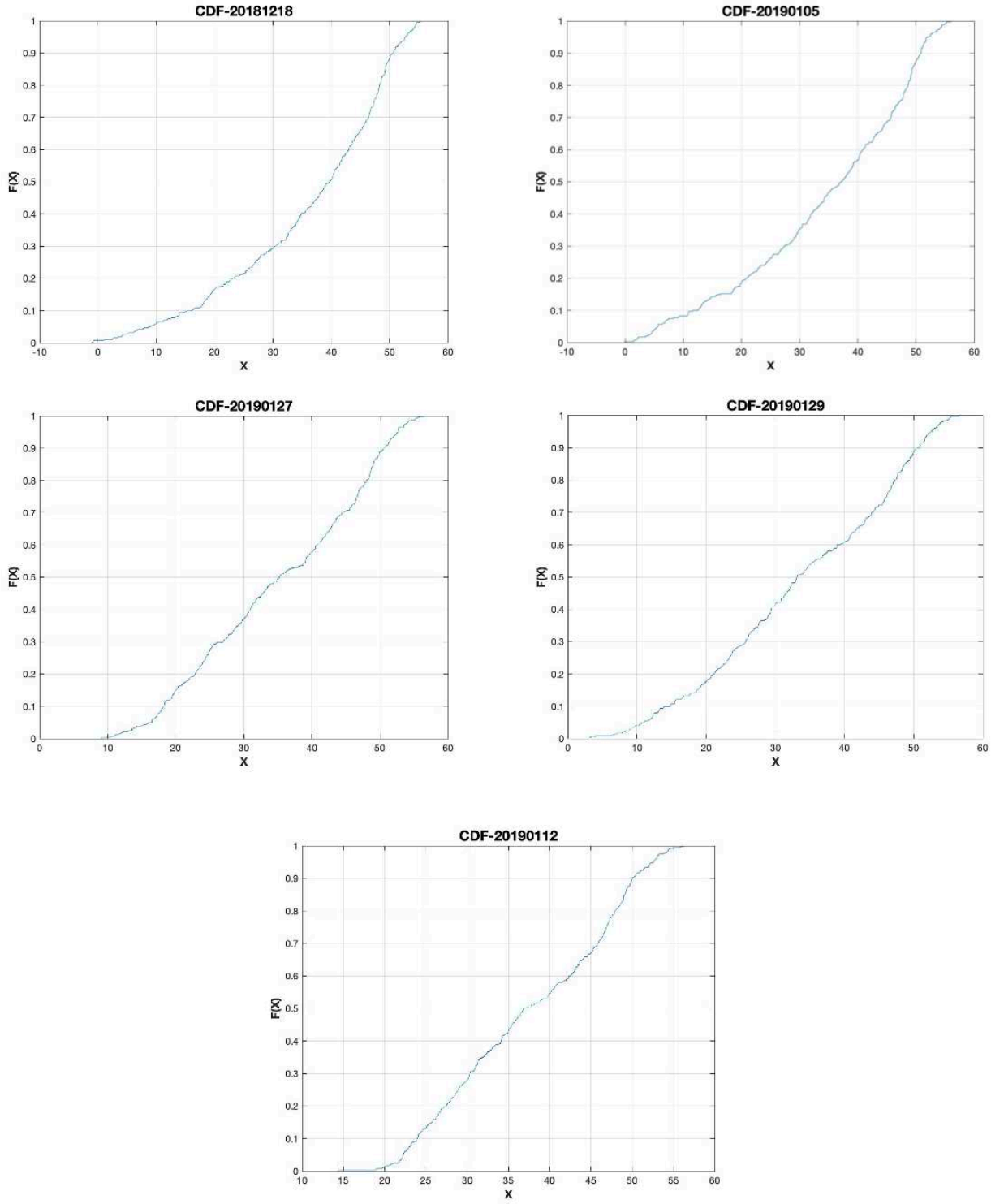

Figure 5.5: CDF of the ground targets with azimuth correction.

Figure 5.6 shows the values of RCA for each precipitation-free case during the RELAMPAGO campaign, where the baseline date is December 31, 2018. As shown in the figure, RCA fluctuated slightly throughout the campaign. After thorough analyses and experiments with RCA obtained for cases in November, December, and January 2018, it was determined that RCA fluctuated significantly when moderate precipitations were present. Furthermore, performance degradation in RCA was observed in cases, in which light rain precipitations were present. For this reason, only precipitation-free dates were selected to ensure high data quality.

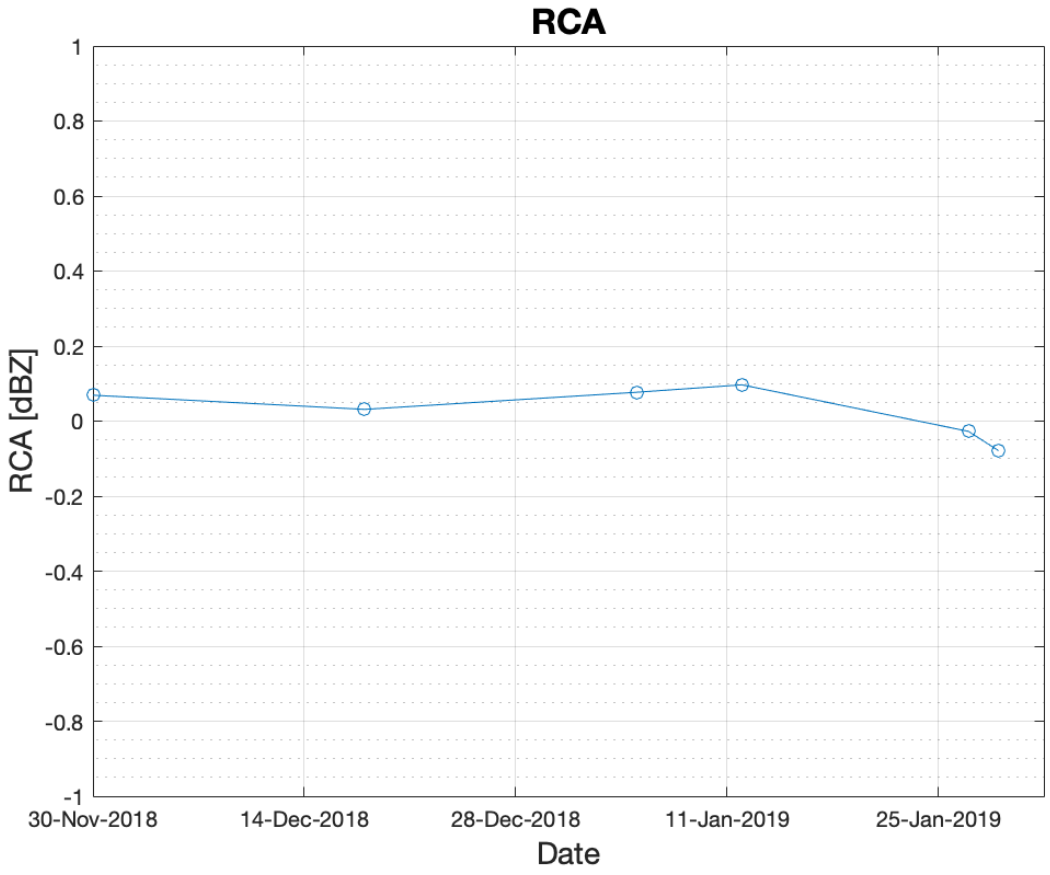

Figure 5.6: RCA values CHIVO radar during the RELAMPAGO campaign with respect to the value of RCA being 0 dBZ on December 31, 2018.

Based on the RCA and the absolute Z bias obtained by the self-consistency principle, the final Z biases for the RELAMPAGO campaign were calculated. Before applying azimuth correction, errors were present up to 1.5 dBZ, however, this was caused by the insufficient number of data points of the ground targets. After the azimuth correction was applied, Z bias fluctuated less than 0.2 throughout the RELAMPAGO campaign. Figure 5.7 shows the final Z biases for each precipitation-free case during the RELAMPAGO campaign.

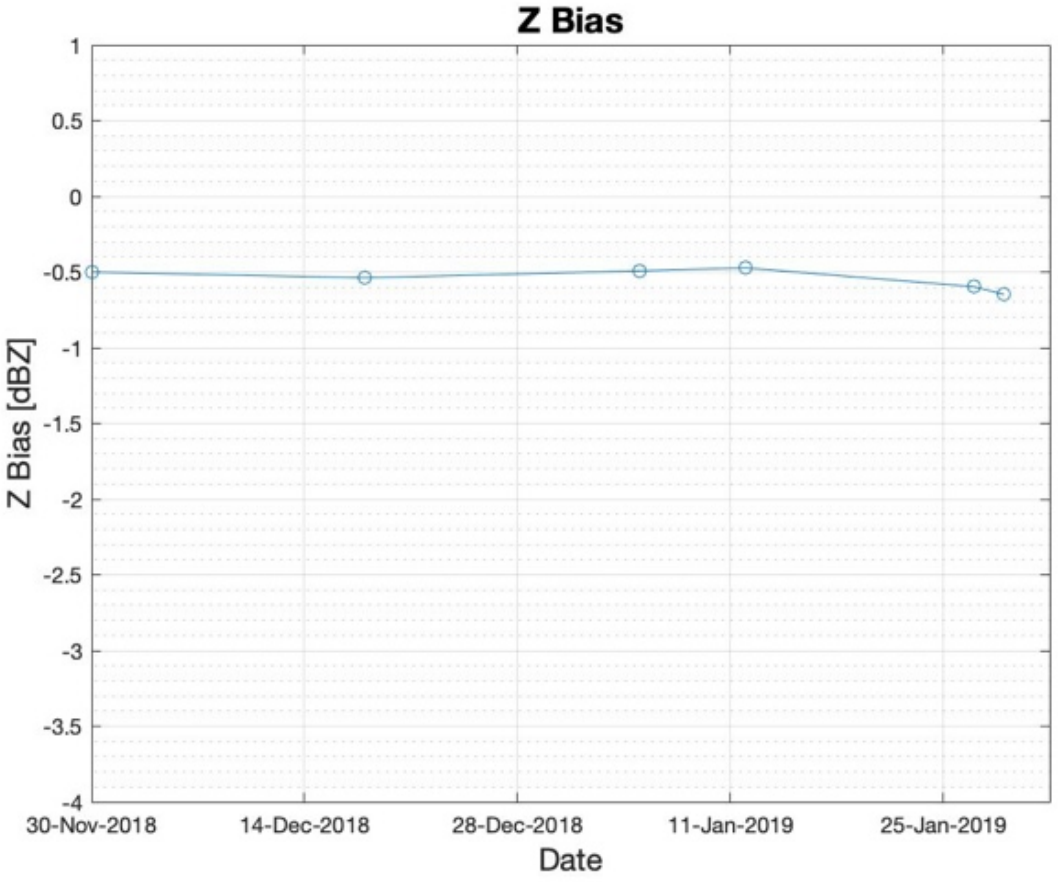

Figure 5.7: Z bias obtained by RCA in combination with the self-consistency principle.

The number of data points within the data sets, which were filtered out with stringent requirements demonstrates that there were enough data points to calculate the mean and median of Z to obtain accurate relative Z bias. Figure 5.8 shows the number of data points for each case after the azimuth data sets were corrected. As shown in the figure, the number of data points

above the 95th percentile was between 34 and 40, which was significantly higher than the number of data points between 10 and 15, which was observed before the azimuth correction was applied. As a result, ensuring enough data points were used to calculate the relative Z bias was crucial to identify the confidence in the results produced by RCA.

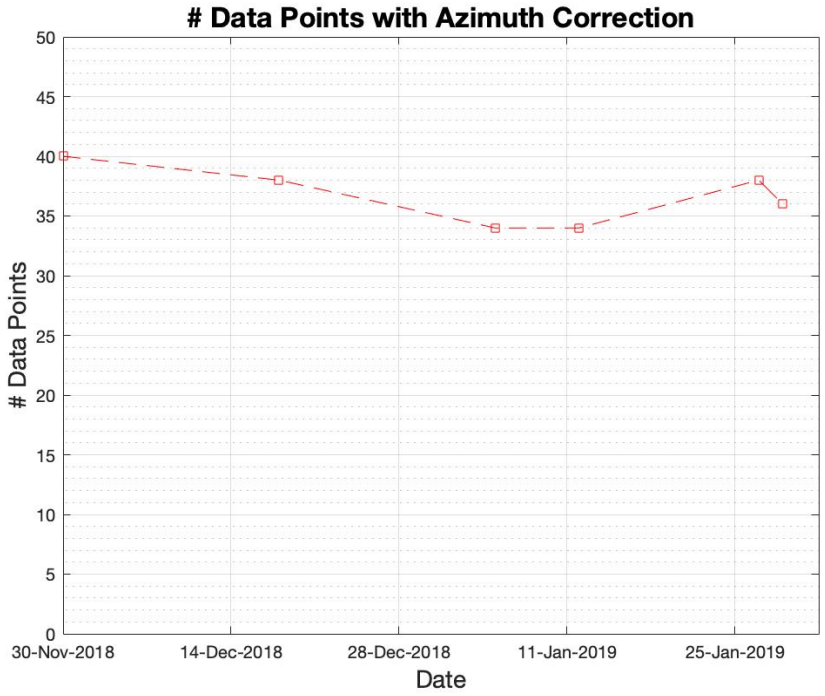

Figure 5.8: The number of data points of the 95th percentile of ground clutter data obtained by cumulative distribution function (CDF) with azimuth correction.

5.5 Summary

As a result, obtaining Z bias using RCA provided more information on the fluctuations of Z on precipitation-free days during the RELAMPAGO campaign. The main advantage of the method was that fixed ground targets could be used, which are easy to be collected and manipulated within datasets.

It was observed that light precipitations degraded the performance of RCA, therefore, the only optimal condition to apply RCA is precipitation-free. Furthermore, azimuth drift degraded

the performance of RCA significantly, therefore, the azimuth correction was a crucial step before RCA was applied to observe the relative Z bias.

Chapter 6

Self-Consistency Principle

6.1 Introduction

The self-consistency principle is used to obtain the absolute Z bias by using pure rain cells as references. The main idea of applying the self-consistency principle is to reconstruct ϕ_{dp} and compare the data to that of measured ϕ_{dp}, and find a value of Z bias that would match both ϕ_{dp}s. To construct ϕ_{dp}, K_{dp} was first constructed from Z and Z_{dr}, and ϕ_{dp} was then constructed from the constructed K_{dp}. When the measured and constructed ϕ_{dp} were compared, the ϕ_{dp} bias was calculated, which would indicate how much of a Z bias was present. By re-calculating ϕ_{dp} by sweeping Z, the optimal value of Z was obtained to minimize ϕ_{dp} bias, which was chosen to be the absolute Z bias. The following constraints were applied to apply the self-consistency principle:1) there must be no precipitation over the radar dome, and 2) the pure light rain cells must be collected within a 50-km range.

6.2 Algorithm Descriptions

Rain cells were carefully chosen by finding ideal rain cells, which were observed by evaluating 2-degree-elevation PPI plots. To avoid collecting melting layers and heavy precipitation, the maximum range was set to 50 km. To ensure pure rain cells are collected, the σ_{hv} minimum threshold was set to 0.9 before K_{DP} was calculated from Z and Z_{dr}. Based on the calculated K_{dp}, ϕ_{dp} was calculated, and the calculated ϕ_{dp} was compared to the measured ϕ_{dp}. To re-calculate the calculated ϕ_{dp}, which would allow it to match well with the measured ϕ_{dp}, Z

was swept to find an optimal Z value that would allow both measured and calculated ϕ_{dp} to match.

6.3 Results & Discussion

Figure 6.1 shows a 2-degree-elevation PPI plot at 03:30:54 UTC on November 30, 2018, during the RELAMPAGO campaign. The black and red arrows correspond to azimuths of 270.782 and 281.818 degrees, respectively. At these azimuths, rain cell data were collected for the ranges of 20 – 50 km and 20 – 40 km, respectively.

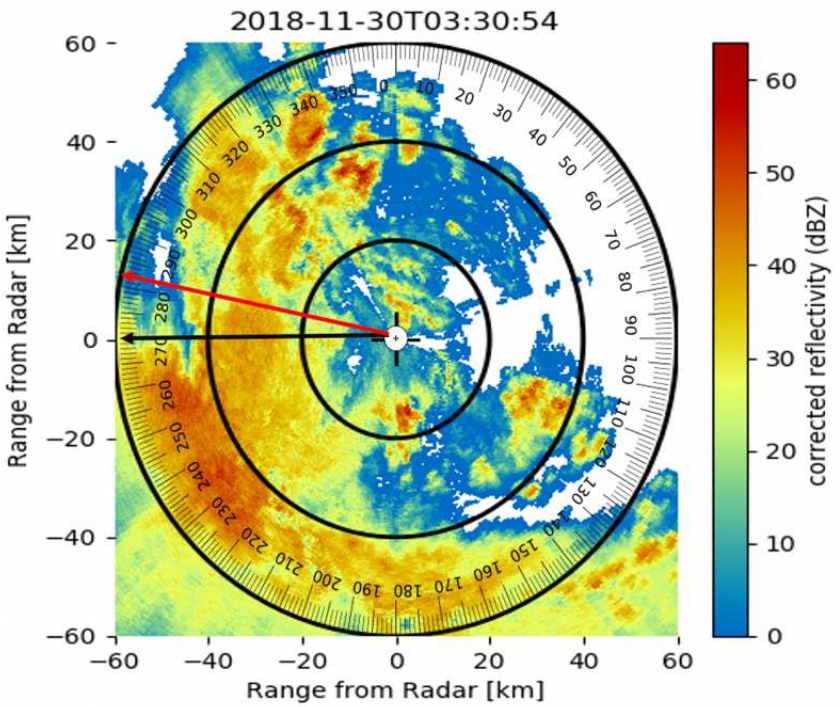

Figure 6.1: A PPI plot for November 30, 2018, 03:30:54 UTC for CHIVO during the RELAMPAGO campaign, where the ideal rain cells, which were used to apply the self-consistency principle are marked by black and red arrows.

Figure 6.2 and Figure 6.3 show Z and Z_{dr} for detected ideal rain media, respectively, along the propagation paths marked by the black and red arrows in Figure 6.1. The parabolic-shaped Z along the propagation path indicates that there are some precipitations present along the propagation path. The value of Z reaching up to approximately 40 dBZ indicated that there were

large-signal returns from the rain media due to moderate precipitations. On the other hand, data points nearby 0 dB up to approximately 3 dB indicated that raindrops in spherical and oblate shapes are present. However, because all the Z data points do not exceed 45 dBZ and the datapoints of Z_{dr} do not exceed 3 dB, it was concluded that there were no hails or ice crystals present. For these reasons, the results on Z and Z_{dr} plots show that the collected data points were only pure rain cells, therefore, were appropriate to be processed.

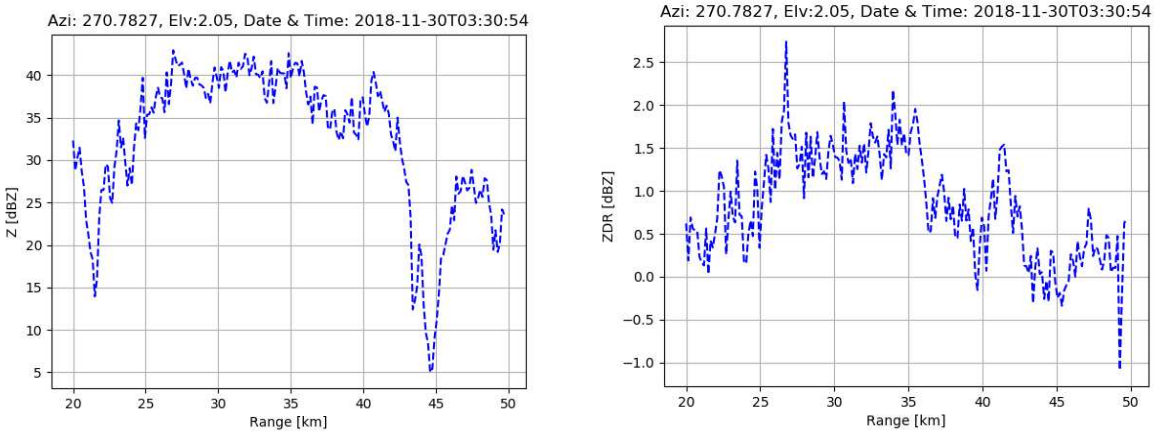

Figure 6.2: Z and Z_{dr} of a rain cell present on November 30, 2018, at an azimuth of 270.783.

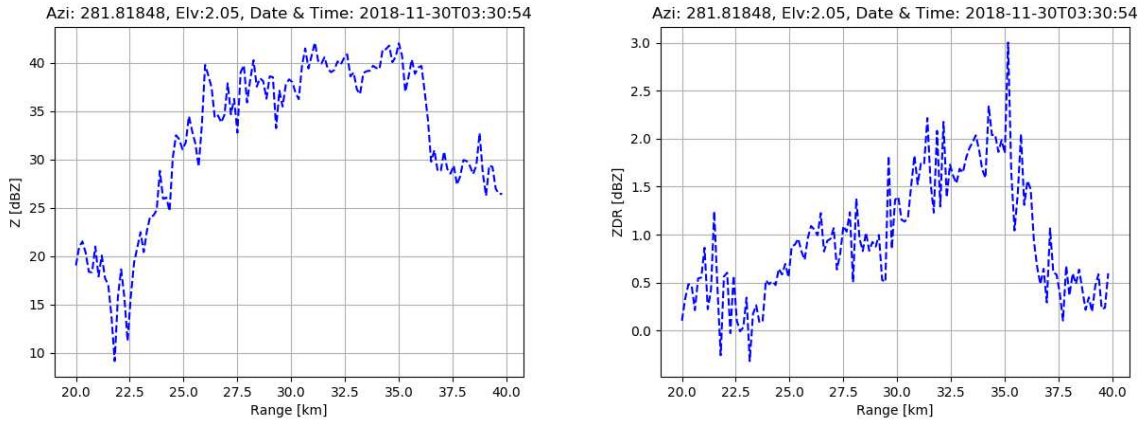

Figure 6.3: Z and Z_{dr} of a rain cell present on November 30, 2018, at an azimuth of 281.818.

Figure 6.4 shows two cases for the measured K_{dp}. Since K_{dp} presents the phase delays occurring at each range location, the parabolic-shaped K_{dp} indicated that rain media were present along the propagation path. Because the denser the rain media the more the phase delays occur,

the amount of phase delay that occurred was seen as significantly higher over the area where the precipitation was present: from 20 to 50 km and from 25 to 40 km at the azimuth of 270.782 and 281.818 degrees, respectively.

The maximum phase delays indicated by K_{dp} occurred at 32.5 and 30 km at the azimuth of 270.782 and 281.818, respectively. The value of K_{dp} at 4.8 and 0.37 deg/km indicated that moderate precipitation was present, and the precipitation did not contain hails. The range of K_{dp} indicated that only the pure rain cells were present in the dataset. The underlying difference between Z_{dr} and K_{dp} was that high Z_{dr} indicated how many large-sized and oblate-shape raindrops were present within a sample volume and K_{dp} indicated how dense the precipitation was. In other words, in theory, sparsely distributed large-sized raindrops would return relatively high Z_{dr} but low K_{dp}, and dense light raindrops would return relatively low Z_{dr} and high K_{dp}. For this reason, comparing Figure 6.2 and 6.3 with Figure 6.4, the value of Z_{dr} was not necessary at its peak at which the peak value of K_{dp} occurred. Comparing the K_{dp} and the Z_{dr} characteristics of the rain medium, it was observed that the rain media included dense raindrops, which included both densely distributed spherical and oblate-shaped raindrops.

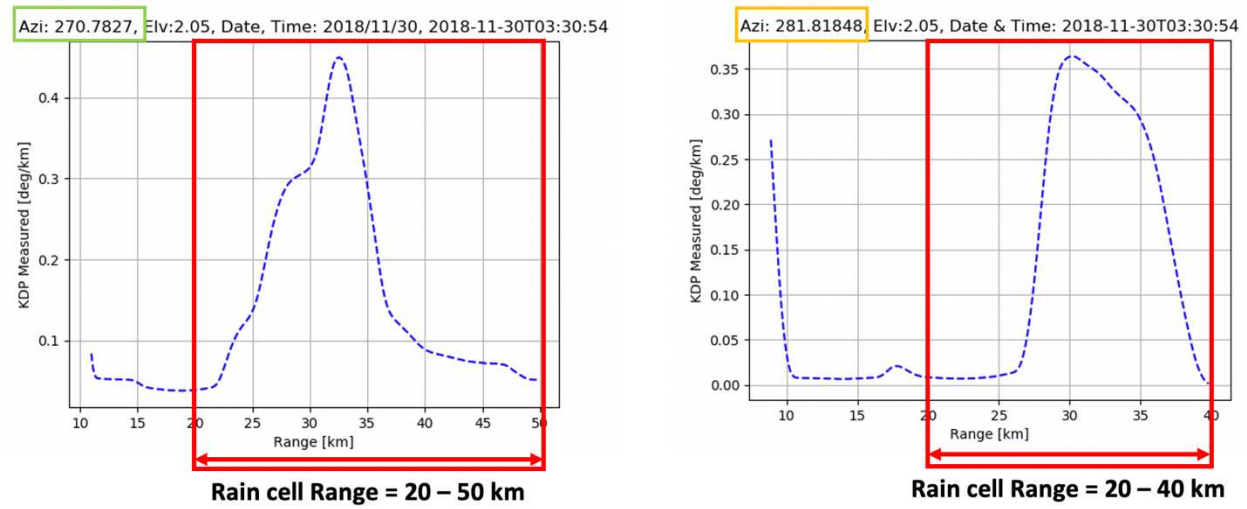

Figure 6.4: Rain cell observed by K_{dp} at fixed-azimuths, and the corresponding target ranges marked by the red squares and arrows, which were used to reconstruct K_{dp} and ϕ_{dp} from Z and Z_{dr}.

After verifying that only the pure rain cells were collected based on observations on the characteristics of Z, Z_{dr}, and K_{dp}, K_{dp} was re-constructed from the datapoints from Z and Z_{dr}. Due to the sensitivity of the C-band CHIVO radar, the initial construction of K_{dp} included many data points that fluctuated significantly along the propagation path. For this reason, the K_{dp} was reconstructed by using a moving-averaging window, which averaged the calculated values of K_{dp} in 5 data points, where each data point was 0.2 km apart from the other, therefore, averaging data points with 1-km resolution. To ensure the high data quality before constructing ϕ_{dp} from K_{dp}, the standard deviation was used to observe fluctuations within the datasets. As a result, K_{dp} was constructed from Z and Z_{dr} as shown in Figure 6.5. The blue line indicates the averaged K_{dp} at each range location and the area marked by the green shades presents the $\pm$ the mean standard deviation along the propagation path. The mean standard deviation of 0.0875 and 0.0764 deg/km at the azimuth of 270.782 and 281.818 degrees, respectively, indicated that the constructed K_{dp} was stable, therefore, was suitable to construct ϕ_{dp}.

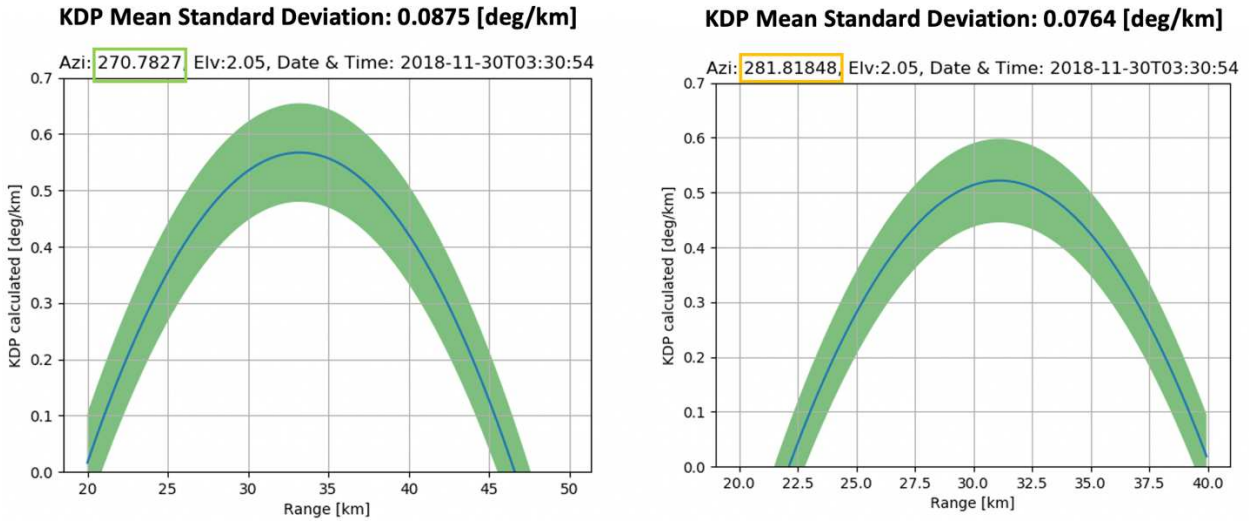

Figure 6.5: K_{dp}, which was constructed by Z and Z_{dr} in combination with the coefficients C, α, and β. Green shades indicate the area covered by $\pm$ standard deviation with respect to the mean K_{dp} marked by the blue line along the propagation path.

To examine the phase delays occurring along the propagation path, the data points from the constructed K_{dp} were used to calculate ϕ_{dp}. The main reason ϕ_{dp} is used to find the optimal point of Z is that ϕ_{dp} allows identifying a mismatch between the measured and constructed ϕ_{dp} easier. If, for example, K_{dp} was used, some variations along the path would be observed, however, identifying how much of the mismatch occurs would be challenging. On the other hand, observing ϕ_{dp}, which presents the accumulation of the phase delays along the propagation path explicitly shows the behavior of the phase delays along the path. Therefore, comparing the measured and the calculated ϕ_{dp} is the most accurate verification process to obtain Z bias.

Figure 6.6 shows the measured and calculated ϕ_{dp} marked by blue and red dashed lines, respectively. The results in Figure 6.6 were obtained by observing how well the calculated ϕ_{dp} matched with the measured ϕ_{dp} while sweeping an input parameter that would be inserted into the Z dataset to construct K_{dp} to construct ϕ_{dp}. In this case, the input variable was swept from -5 to +5 dBZ, and the value of the variable that matched the constructed and the measured ϕ_{dp} the best was -0.5 dB. The more data points were available from the precipitation, the more accurate

the data points of the ϕ_{dp} became. As shown in Figure 6.6, ϕ_{dp} from 27.5 to 40 km and from 30 to 36 km at the azimuth of 270.782 and 281.818 degrees matched very well while minor mismatch occurred out of the range. This was due in part to the lack of data points and minor noise present in the Z and Z_{dr} datasets, which were used to construct K_{dp} and ϕ_{dp}.

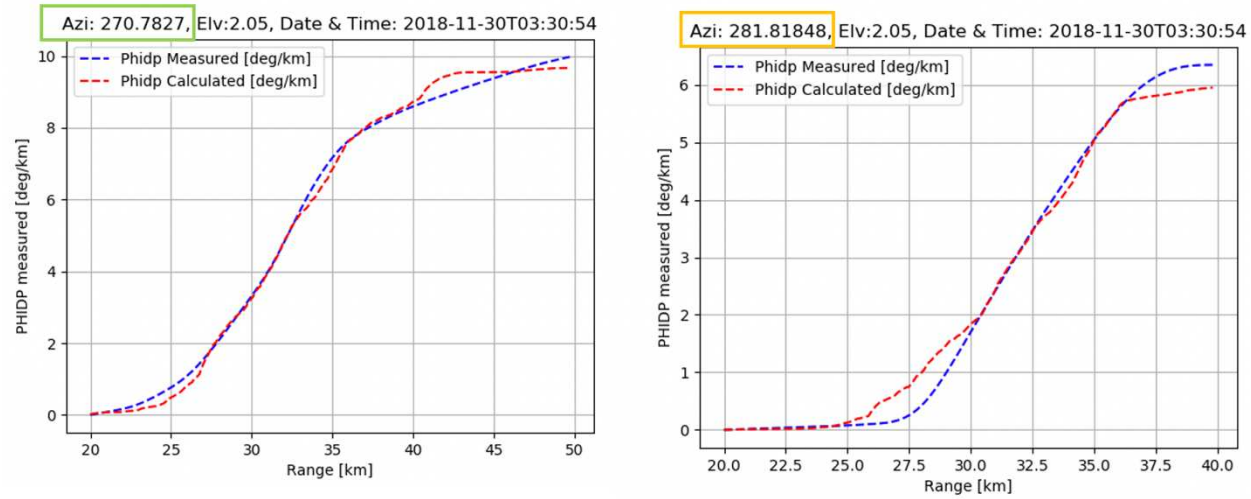

Figure 6.6: Constructed and measured ϕ_{dp} marked by red and blue, respectively along the propagation path.

Arias and Chandrasekar [25] performed a calibration study of the CSU-CHIVO radar with Dual-frequency Precipitation Radar (DPR) abroad the GPM satellite following the procedure described in [25-26]. The bias between the DPR Ku-band and the CSU-CHIVO was 0.14 [25], which indicated that the Z from Ku-band PR from GPM yielded higher values. In other words, the CHIVO radar returned Z values lower than the value of Z from Ku-band PR. On the other hand, the Z bias obtained by applying the self-consistency principle was -0.5. Both results show that CHIVO radar is negatively biased. Supposing that the Z bias obtained by the self-consistency principle is correct, the Z bias of Ku-band PR is approximately -0.36 dBZ. Therefore, considering that the natural bias of Z is 0.2 dBZ and the bias of Ku-band PR less than 1 dBZ [25], the Z bias of -0.5 obtained by the self-consistency principle is consistent with the results from the cross-validation work by Arias and Chandrasekar [25]. Figure 6.7 shows the

comparison of Z between Ku-band PR and CHIVO [25] and the absolute Z bias obtained by applying the self-consistency principle.

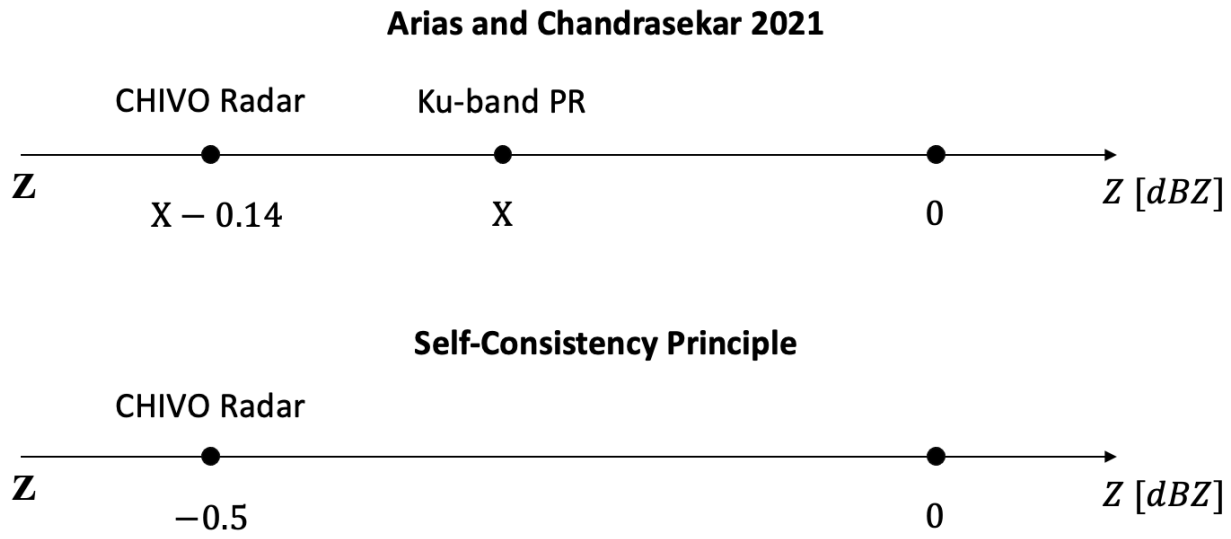

Figure 6.7: Comparison of Z between CHIVO radar and Ku-band PR by Arias and Chandrasekar (top) and the Z bias obtained by applying the self-consistency principle (bottom).

6.4 Summary

In this chapter, it was demonstrated that following all the requirements correctly would obtain the absolute Z bias by applying the self-consistency principle. The most important part was to collect and verify the ideal rain cell by analyzing the data using Z, Z_{dr}, K_{dp}, and ϕ_{dp} characteristics. It was shown that the Z data points from the ideal rain media would form a parabolic-shaped graph along the propagation path, where rain media were present between both endpoints of the parabolic-shaped plot. The value of Z datapoints ranged up to 40 dBZ, which indicated that moderate precipitation was present. Z_{dr} data points were located between 0 and 3 dB, which described the rain media that consisted of both spherical-shaped raindrops and oblate-shaped raindrops, which are in bigger sizes. K_{dp} described how much phase delay occurred along the propagation path at each range location. The denser the raindrops the rain media contain, the

more phase delays occur, therefore, K_{dp} along the propagation path was parabolic-shaped as it was for Z. However, it was important to note that the data points with high values of Z_{dr} did not necessarily return high values of K_{dp}, because in theory, sparsely distributed bigger and oblate-shaped raindrops would return relatively low K_{dp} than densely distributed smaller raindrops. ϕ_{dp} represents the accumulation of the phase delays along the propagation path. Since the rain cells datapoints were collected between two endpoints, where the rain cell started and ended, ϕ_{dp} formed a curve that increased along the path and stabilizes at the endpoint. After the pure rain cells were verified using Z, Z_{dr}, and K_{dp}, the measured and constructed ϕ_{dp}s were compared, which mismatched, therefore, indicating that there was a Z bias present according to the self-consistency principle. Theoretically, if there is no Z bias, both of the ϕ_{dp}s would match perfectly, however, a minor mismatch of the ϕ_{dp}s indicated that there was a minor Z bias present in CHIVO radar. When matching the measured and the constructed ϕ_{dp}s with an arbitrary Z bias input, the matching of the ϕ_{dp}s for a range, where the number of data points from Z and Z_{dr} was sufficient. As a result, identifying pure rain cells using Z, Z_{dr}, and K_{dp}, and matching the measured and the constructed ϕ_{dp}s proved to be robust in obtaining the absolute Z bias.

Furthermore, it was observed that cross-validation work, which compares the Z bias obtained by GPM would further verify the accuracy of the Z bias obtained by using the self-consistency principle.

Chapter 7

Summary and Future Work

7.1 Summary

As presented in this thesis, the four radar calibration techniques, which utilized ground targets, light rain media, and the sun as a reference source improved CHIVO radar data quality significantly. It was demonstrated that the calibration algorithms could be applied successfully if the operational and scanning strategies were optimized to capture a variety of precipitation events, solar rays, and ground targets. Furthermore, most results from RCA showed that azimuth correction was a critical task to improve its performance because of the ground targets being location dependent. Furthermore, the vertical-pointing scanning strategy allowed Z_{dr} bias to be obtained by vertical-pointing analysis along with Z versus Z_{dr} dispersion analysis. Since ideal rain cells were difficult to be found, applying the self-consistency principle to obtain Z bias was very limited. For this reason, RCA was applied to observe changes in Z from fixed-ground targets to accompany the results obtained by the self-consistency principle. As a result, combining the self-consistency principle and RCA to obtain Z bias for both precipitation-free days and days with precipitation produced abundant results for Z bias for the RELAMPAGO campaign.

7.2 Future Work

Although applying the four calibration algorithms to CHIVO radar data improved the data quality significantly, there remains future work, which would further improve the data quality. Because the data analyses were conducted based on the data collected by one ground

radar, cross-validation work, which would combine analyses on data collected by other radars such as GPM and ground radars at different frequencies can be conducted. This cross-validation work would provide more information on the robustness of the radar calibration algorithms by providing abundant results from applying the radar calibration algorithms presented in this thesis. It would be more reasonable to deploy a network of ground radars, which would have overlapped areas to be scanned. Applying the calibration techniques to the different radars could produce more results to be compared, therefore, more validation work could be completed to further improve the data quality.

Bibliography

[1] V. N. Bringi and V. Chandrasekar Bringi, 2001: *Polarimetric Doppler Weather Radar: Principles and Applications.* Cambridge University Press.

[2] W. Stephen et al., 2021: A Storm Safari in Subtropical South America. *American Meteorological Society*., 1641-1644.

[3] Trapp, J. Robert et al., 2020: Multiple-platform and multiple-Doppler radar observations of a supercell thunderstorm in South America during RELAMPAGO. *Monthly Weather Review.*, 148.8, 3225-3241.

[4] A. Dutta, V. Chandrasekar, and S. K. Biswas, 2019: Spectral polarimetry for microphysical studies of rain and hail during Relampago campaign-initial results. *AGU Fall Meeting Abstracts*., A53U-3046.

[5] Schumacher, S. Russ et al., 2021: Convective-storm environments in subtropical South America from high-frequency soundings during RELAMPAGO-CACTI. *Monthly Weather Review.,* 149.5, 1439-1458.

[6] S. K. Biswas, V. Chandrasekar, S. Sahoo, and A. K. Lakshmi, 2022: Study of A Convective Event During The Relampago Field Experiment Using Spectral Polarimetry. *IGARSS 2022 - 2022 IEEE International Geoscience and Remote Sensing Symposium*.

[7] R. Cifelli, V. Chandrasekar, S. Lim, Patrick C Kennedy, Y. Wang, and S. A. Rutledge, 2011: A new dual-polarization radar rainfall algorithm: Application in Colorado precipitation events. *Journal of Atmospheric and Oceanic Technology.*, 28(3):352–364.

[8] H. Chen, V. Chandrasekar, and R. Bechini, 2017: An improved dual-polarization radar rainfall algorithm (drops2.0): Application in NASA iFloods field campaign. *Journal of Hydrometeorology.*, 18(4): 917–937, 2017.

[9] S. K. Biswas, R. Cifelli, and V. Chandrasekar, 2020: Improving Quantitative Precipitation Estimation by X-Band Dual-Polarization Radars in Complex Terrain Over the Bay Area in California, USA. *IGARSS 2020 - 2020 IEEE International Geoscience and Remote Sensing Symposium*., 5411-5414, doi: 10.1109/IGARSS39084.2020.9323239.

[10] S. K. Biswas, R. Cifelli, and V. Chandrasekar, 2018: Evaluation of Quantitative Precipitation Estimation by S-Band Radar in complex terrain over the Feather River basin in California, USA. *AGU Fall Meeting Abstracts*.

[11] G. S. Jackson, W. A. Petersen, W. Berg, C. Kidd, R. F. Stocker, D. B. Kirschbaum, R. Kakar, S. A. Braun, G. J. Huffman, T. Iguchi, et al., 2017: The global precipitation measurement (GPM) mission for science and society. *Bulletin of American Meteorological Society*., 98(8):1679–1695.

[12] S. K. Biswas and V. Chandrasekar, 2017: Cross validation of observations from GPM dual-frequency precipitation radar with S-band ground radar measurements over the Dallas: Fort Worth region. *2017 IEEE International Geoscience and Remote Sensing Symposium (IGARSS)*., 2085-2088, doi: 10.1109/IGARSS.2017.8127393.

[13] S. K. Biswas, M. Le, and V. Chandrasekar, 2017: Identification of snow from GPM-DPR observations and cross validation with S-band ground radar dual polarization measurements. *2017 General Assembly and Scientific Symposium of the International Union of Radio Science (URSI GASS).,* 1-3.

[14] V. Chandrasekar, S. K. Biswas, M. Le, and H. Chen, 2018: Cross Validation of Raindrop Size Distribution Retrievals from GPM Dual-frequency Precipitation Radar Using Ground-based Polarimetric Radar. *IGARSS 2018 - 2018 IEEE International Geoscience and Remote Sensing Symposium*., 8335-8338, doi: 10.1109/IGARSS.2018.8518881.

[15] V. N. Bringi, T. D. Keenan, and V. Chandrasekar, 2001: Correcting C-band radar reflectivity and differential reflectivity data for rain attenuation: a self-consistent method with constraints. *Geoscience and Remote Sensing.*, 39, No. 9.

[16] T. V. Jacques, E. L. Bouar, and E. Obligis, 1998: The rain profile algorithm applied to polarimetric weather radar. *CETP-UVSQ, Velizy France*.

[17] K. V. Beard and C. Chuang, 1987: A new model for the equilibrium shape of raindrops. *J. Atmos. Sci.,* 44, 11, 1509-1524.

[18] E. Gorgucci, V. Chandrasekar, V. N. Bringi, and G. Scarchilli, 2001: Estimation of raindrop size distribution parameters from polarimetric radar measurements. *2002 American Meteorological Society.*

[19] Y. Liu, V. N. Bringi, and M. Maki, 2006: Improved rain attenuation correction algorithm radar reflectivity and differential reflectivity with adaptation to drop shape model variation. *Department of Electrical and Computer Engineering, Colorado State University, Fort Collins, CO.*

[20] S. Lim and V. Chandrasekar, 2016: A robust attenuation correction system for reflectivity and differential reflectivity in weather radars. *IEEE transactions on geoscience and remote sensing.,* 54, No. 3.

[21] J. Tan, D. H. O. Bebbington, and A. R. Holt, 2009: Theoretical studies of differential propagation phase shift in meteorological polarization diversity radars at centimeter wavelengths. *University of Essex, UK.*

[22] W. Chen, J. He, Z. Shi, and R. Liao, 2019: Quality control of differential phase of dual polarization radar based on Kalman filter algorithm. *National Key R&D Program of China.*

[23] Q. Xia, H. Chen, J. He, W. Zhang, and Z. Yao, 2019: Differential phase processing and data quality control for polarimetric weather radar in southern China. *Photonics & Electromagnetics Research Symposium.*

[24] T. Otto, W. Herman, and J. Russchenberg, 2011: Estimation of specific differential phase and differential backscatter phase from polarimetric weather radar measurements of rain. *IEEE Geoscience and Remote Sensing Letters*, 8, No. 5.

[25] Ivan Arias and V. Chandrasekar, 2021: Cross-Validation of the Network of Ground-Based Radar with GPM during the Remote Sensing of Electrification, Lightning, and Mesoscale/Microscale Processes with Adaptive Ground Observations (RELAMPAGO) Field Campaign. *Journal of the Meteorological Society of Japan,* 1423-1437, doi:10.2151/jmsj.2021-069.

[26] Schwaller, R. Mathew, and K. R. Morris, 2011: A ground validation network for the global precipitation measurement mission. *Journal of Atmospheric and Oceanic Technology.,* 28, No. 3, 301-319.

[27] S. K. Biswas and V. Chandrasekar, 2018: Cross-Validation of Observations between the GPM Dual-Frequency Precipitation Radar and Ground Based Dual-Polarization Radars. *Remote Sensing.,* 10, No. 11: 1773. https://doi.org/10.3390/rs10111773.

[28] T. Schuur, A. Ryzhkov, and D. Clabo, 2005: Climatological analysis of DSDs in Oklahoma as revealed by 2D-video disdrometer and polarimetric WSR-88D. *Proc. 32nd Conf. Radar Meteorol*., 1-7.

[29] J. C. Hubbert and F. Pratte, 2006: Differential Reflectivity Calibration for NEXRAD. *NCAR/EOL, Boulder, CO.*

[30] B. Wolff, A. Marks, and A. Petersen, 2014: General Application of the Relative Calibration Adjustment (RCA) Technique for Monitoring and Correcting Radar Reflectivity Calibration. *Journal of Atmospheric and Oceanic Technology.,* 32, 496-506, doi: 10.1175/JTECH-D-13-00185.1.

[31] G. Scarcbilli, E. Gorgucci, and V. Chandrasekar, 1996: Self-Consistency of polarization diversity measurements of rainfall. *Geoscience and Remote Sensing.*, Vol. 34, No. 1.

[32] M. Trabal, E. Gorgucci, and V. Chandrasekar, 2014: Evaluation of the self-consistency principle for calibration of the CASA radar network using properties of the observed precipitation medium. *Geoscience and Remote Sensing.*, 52, No. 1.